UTILIZATION OF NARROWBAND AND WIDEBAND RADIO FREQUENCY MEASUREMENTS FOR DEVICE-FREE LOCALIZATION

by

Merrick K. McCracken

A dissertation submitted to the faculty of
The University of Utah
in partial fulfillment of the requirements for the degree of

Doctor of Philosophy

Department of Electrical and Computer Engineering

The University of Utah

December 2013

The University of Utah Graduate School

STATEMENT OF DISSERTATION APPROVAL

The dissertation of **Merrick K. McCracken**

has been approved by the following supervisory committee members:

Neal Patwari	, Chair	**10/31/2013** Date Approved
Rong Rong Chen	, Member	**10/31/2013** Date Approved
Behrouz Farhang	, Member	**10/31/2013** Date Approved
Thomas Schmid	, Member	**10/31/2013** Date Approved
Suresh Venkatasubramanian	, Member	**10/31/2013** Date Approved

and by **Gianluca Lazzi** , Chair/Dean of

the Department/College/School of **Electrical and Computer Engineering**

and by David B. Kieda, Dean of The Graduate School.

ABSTRACT

This work seeks to improve upon existing methods for device-free localization (DFL) using radio frequency (RF) sensor networks. Device-free localization is the process of determining the location of a target object, typically a person, without the need for a device to be with the object to aid in localization. An RF sensor network measures changes to radio propagation caused by the presence of a person to locate that person. We show how existing methods which use either wideband or narrowband RF channels can be improved in ways including localization accuracy, energy efficiency, and system cost. We also show how wideband and narrowband systems can combine their information to improve localization.

A common assumption in ultra-wideband research is that to estimate the bistatic delay or range, "background subtraction" is effective at removing clutter and must first be performed. Another assumption commonly made is that after background subtraction, each individual multipath component caused by a person's presence can be distinguished perfectly. We show that these assumptions are often not true and that ranging can still be performed even when these assumptions are not true. We propose modeling the difference between a current set of channel impulse responses (CIR) and a set of calibration CIRs as a hidden Markov model (HMM) and show the effectiveness of this model over background subtraction.

The methods for performing device-free localization by using ultra-wideband (UWB) measurements and by using received signal strength (RSS) measurements are often considered separate topic of research and viewed only in isolation by two different communities of researchers. We consider both of these methods together and propose methods for combining the information obtained from UWB and RSS measurements. We show that using both methods in conjunction is more effective than either method on its own, especially in a setting where radio placement is constrained.

It has been shown that for RSS-based DFL, measuring on multiple channels improves localization accuracy. We consider the trade-offs of measuring all radio links on all channels and the energy and latency expense of making the additional measurements required when sampling multiple channels. We also show the benefits of allowing multiple radios to transmit simultaneously, or in parallel, to better measure the available radio links.

CONTENTS

LIST OF TABLES

CHAPTER 1

INTRODUCTION

Device-free localization (DFL) is the process of determining the location of a target object, typically a person, without the need for a device to be with the object to aid in localization. Knowing where a person or multiple people are located in a room or building is valuable information for building security. The information provided by device-free localization can also be used to help caretakers of the elderly by knowing their movements within their home and their inactivity as well, which could signal their need for help. In either of these scenarios, it is very impractical to require the people to carry with them a device that would be used to aid localization.

Localization is performed by employing the information provided by sensors placed such that the the object or person can be located in a target area or region. The sensors detect and quantify changes in the environment caused by the person's presence or movement. By knowing or modeling how a person may change sensor data as a function of the person's location, an estimate of the person's location can be made using the available sensor data.

Device-free localization can be done with a number of different sensing techniques including cameras and image processing [1], reading radio-frequency identification (RFID) tags [2], and wideband [3] and narrowband [4]–[7] radio frequency (RF) sensing as will be discussed in Sections 1.1.1 and 1.1.2, respectively.

1.1 Radio Frequency Sensing

The human body affects radio propagation, both in narrowband and in wideband transmissions. For a radio signal there exist multiple transmission paths, or multipath, between radio transmitters and receivers. The presence of a person can both cause new multipath to form, from reflection or refraction, and block or attenuate existing multipath. The presence of a person, therefore, causes a change in the signal arriving at the receiving radio compared to the signal that would have arrived had the person not been there.

1.1.1 Wideband Effects

For wideband or ultra-wideband (UWB) transmissions, a time-domain representation of the arriving signal is often available from the receiving UWB radio. Assume that an UWB transmitter sends pulse $\delta(t)$. Due to multipath propagation, the received signal is described by

$$h(t) = \sum_i \alpha_i \delta(t - \tau_i), \tag{1.1}$$

where α_i and τ_i are the complex amplitude and time delay of the ith path, respectively. The value τ_0 corresponds to the UWB impulse following the line-of-sight path between the two radios, which are separated from each other by a distance on the order of meters or more. As the time progresses, more UWB impulses arrive at the receiver that reflected off of objects and scatterers in the environment. These impulses traveled paths longer than the line-of-sight path, each with its corresponding τ_i.

The receiver radio approximately measures the channel impulse response convolved with the pulse shape. Fig. 1.1 is an example of how the transmitted pulse may follow many different paths to arrive at the receiver.

The number of multipath components seen by the receiver depends on the environment around the radios. The presence of a person will have two primary effects. The first is that the person's body will cause a new multipath impulse to arrive at the receiver. When a person appears at point x_0 in the environment with the transmitter at x_t and receiver at x_r, he causes an additional path with path length $\|x_t - x_0\| + \|x_0 - x_r\|$, where $\|\cdot\|$ is the L^2 norm. This is true if we assume the impulse will reflect or bounce only off of the person and no other object while traveling from the transmitter to the receiver. This path length is greater than the line-of-sight path length. The difference in length between these two paths is the excess path length.

The excess path length of the multipath component caused by the person can be used to estimate the sum of the distances to each radio from the person's location. The sum of these distances together is known as the bistatic range. The delay associated with this new multipath component is τ_*, which we refer to as the *bistatic delay*. The second effect the person has is that it will affect existing multipath. As illustrated in Fig. 1.2, the presence of a person will affect multipath components that the receiver would have measured had the person not been there. The person's body can affect any multipath component whose path

length is greater than or equal to that path length of the person's multipath component, that is, the person affects many α_i for $\tau_i \geq \tau_*$.

1.1.2 Narrowband Effects

Narrowband radio signals are similarly affected by the presence of a person's body. Unlike UWB impulse measurements, however, a time-domain representation of the arriving signal is unavailable. For packet-based radio protocols, such as 802.15.4, a link quality measurement is often provided by the receiving radio for each packet reception. This measurement is often a received signal strength (RSS) measurement. This RSS measurement can be used to determine the channel fading, or fade level, or the wireless communication channel.

Similar to UWB measurements, received narrowband signals can be modeled as

$$H = \sum_i \alpha_i e^{jf_c\tau_i}. \tag{1.2}$$

This is similar to equation (1.1) but considered in the frequency domain, where $\delta(t - \tau_i)$ becomes $e^{jf_c\tau_i}$ in the frequency domain. This is done because the time required to transmit the narrowband signals is much greater than individual multipath delays, which is unlike UWB measurements. Therefore, we can consider all multipath as if they are arriving simultaneously. The RSS measurements are the received power and are proportional to $|H|^2$. RSS is measured in units of dBm.

These arriving multipath can interfere constructively or destructively. The level of constructive or destructive interference is know as fading or is describe by the fade level of the signal. This interference can be illustrated in the following way.

In Figs. 1.3 and 1.4, the individual complex amplitudes of each arriving multipath component are shown on the complex plane. In both figures, the black arrows represent the complex amplitudes of individual multipath components and the red arrow represents the sum of the individual components. In Fig. 1.3, the components interfere constructively. A link with a received signal such as this would be considered an antifade link, or a link where there is little or no fading. The received signal is strong, and effects to the link's multipath components generally cause the RSS value to decrease. In Fig. 1.4, the components interfere destructively. This signal would be considered a deep-fade link, or a link where the fading is strong. Changes to the multipath components may cause the RSS value to increase or decrease in value. It is because RSS is measured in a log scale that there is a higher variability is RSS measurements for deep-fade links than for those in antifade links.

Generally, when a person affects one or more multipath components of an antifade link, the overall signal is attenuated. For a deep-fade link, however, it becomes more likely that an affected multipath could result in constructive interference and an increase in RSS. The changes in RSS values relative to their fade level, which is measured during a calibration period, can be used to determine where a person is within the environment. This is done by employing a model of how the person affects a link's RSS measurements depending on where the person is and what the fade level of the link is. This effect has been modeled in a number of ways [5], [8]–[10].

1.2 Radio Tomographic Imaging

Radio tomographic imaging (RTI) is the process of estimating the changes to the RF propagation field. These changes are estimated over a discretized target area, which is the area where the radio sensors can effectively monitor the changes caused by the presence of a person. Each discretized partition of the target area corresponds to one pixel in the localization image. Image maxima indicate possible person locations.

Critical to performing RTI is a model of how a person affects radio propagation as a function of the person's location relative to the link. For narrowband systems, the measured changes to RSS values serve as a measure of changes in radio propagation. A number of different models of how a person affects radio propagation have been proposed based on changes in attenuation [5], signal variance [8], and based on both the change in attenuation and the direction of change [9].

Instead of applying a model of how a link is affected by the presence of a person, an alternative method for estimating a person's location is by using fingerprint-based methods [4], [11]. These methods require additional training data beyond a calibration measurement of the empty environment. For these methods, training measurements are made for many discrete locations where the person may be by having a person stand in each of these locations while measurements are made. Then when a person's location estimate is to be made, the current measurements are compared to the set of training data. The training data that most closely resemble the measured data give their corresponding training location as the estimated location of the person. These methods require much more training data, which grow linearly with the number of discrete training locations and exponentially with the number of possible people in the target environment. New training data may also be necessary if the environment changes significantly.

For ultra-wideband systems, changes in the radio propagation field for RTI are modeled by changes to the received, time-domain, channel impulse responses (CIR). This information

is used to estimate the bistatic range of people or objects affecting the CIR, producing iso-range contours around the UWB radios. These contours, shaped as ellipses, are estimates of where changes occur in the radio propagation field due to the presence of a person. A number of ways to perform localization using UWB measurements is further discussed in Section 2.2.7.

1.3 Contributions

A common assumption in ultra-wideband research is that to estimate the bistatic delay or range, "background subtraction" must first be performed. This means that a prior measurement of the CIR is subtracted from any current CIR measurement. These prior measurements are presumed to be made when the area is empty (*i.e.*, with a static background). Some work in UWB-based impulse response radar assumes that background subtraction is completely effective in removing the response due to the static environment [12]–[15]. Another assumption commonly made is that after background subtraction, each individual multipath component caused by a person's presence can be distinguished perfectly from the impulses caused by other people and the environment [13], [14]. In Chapter 2, we show that these assumptions are often not true and that ranging can still be performed even when these assumptions are not true.

The methods for performing device-free localization by using UWB measurements and by using RSS measurements are often considered a separate topic of research and viewed only in isolation by two different communities of researchers. In Chapter 3, we consider both of these methods together and propose methods for combining the information obtained from UWB and RSS measurements. We show that using both methods in conjunction is more effective than either method on its own, especially in a setting where radio placement is constrained.

It has been shown that for RSS based DFL, measuring on multiple channels improves localization accuracy [9], [10]. In Chapter 4, we consider the trade-offs of measuring all radio links on all channels and the energy and latency expense of making the additional measurements required when sampling multiple channels. This work can be used to allow for large-scale deployed systems of RF sensors to use multiple channels simultaneously.

The following publications are a result of this work.

- M. McCracken and N. Patwari, "Hidden Markov Estimation of Bistatic Range from Cluttered Ultra-wideband Impulse Responses," in 2nd IEEE Topical Meeting on Wireless Sensors and Sensor Networks (WiSNet 2012), 2012, pp. 17-20. [16]

- M. McCracken and N. Patwari, "Hidden Markov Estimation of Bistatic Range from Cluttered Ultra-wideband Impulse Responses," IEEE Transactions on Mobile Computing, vol. PP, no. 99, pp. 1-1, 2013. [3]

- M. McCracken, M. Bocca, and N. Patwari, "Joint Ultra-wideband and Signal Strength-based Through-building Tracking for Tactical Operations," in 2013 IEEE International Conference on Sensing, Communications and Networking (SECON), 2013, pp. 309-317. [17]

- M. McCracken, M. Bocca, and N. Patwari. "Selection of Links in Multichannel RSS Measurements for Radio Tomography", (to be submitted to arxiv.org and to be included in "Large Scale, Device Free Localization" by the A. Luong, M. McCracken, M. Bocca, and N. Patwari to be submitted to 2014 IEEE International Conference on Sensing, Communications and Networking (SECON)).

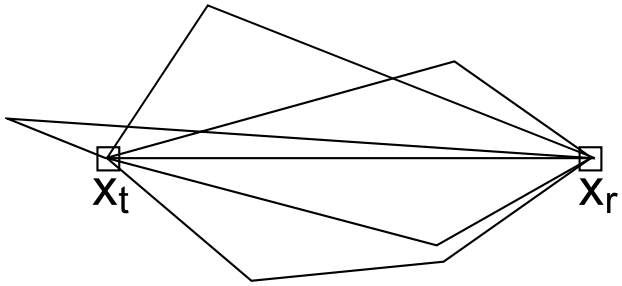

Figure 1.1. The transmitted radio signal takes many paths to arrive at the receiving radio due to the environment.

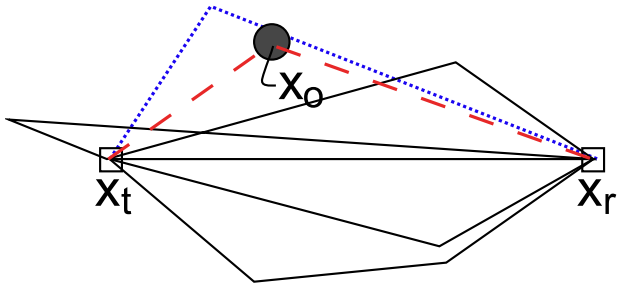

Figure 1.2. The presence of a person in the environment both creates new multipath signals and affects existing multipath signals. How the signal is affected depends on the signal arriving at the receiver without the presence of a person and on where the person is within the environment.

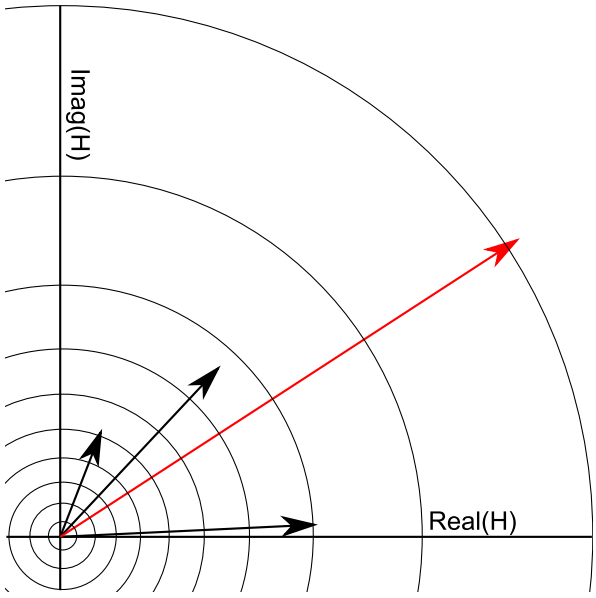

Figure 1.3. Multipath components arrive at the receiver with amplitudes and phase offsets such that the overall received signal strength is high due to constructive interference. These are antifade links. Magnitude contours are drawn on a log scale.

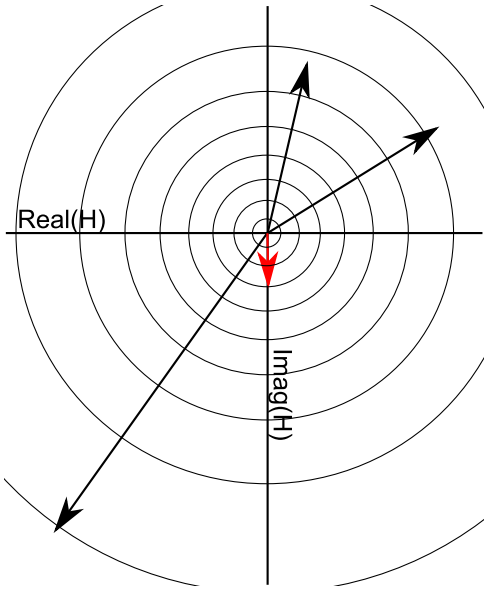

Figure 1.4. Multipath components arrive at the receiver with amplitudes and phase offsets such that the overall received signal strength is very low due to destructive interference. These are deep-fade links. Magnitude contours are drawn on a log scale.

CHAPTER 2

ESTIMATION OF BISTATIC RANGE FROM CLUTTERED ULTRA-WIDEBAND IMPULSE RESPONSES

UWB multistatic radar can be used for target detection and tracking in buildings and rooms. Target detection and tracking relies on accurate knowledge of the bistatic delay. Noise, measurement error, and the problem of dense, overlapping multipath signals in the measured UWB CIR all contribute to make bistatic delay estimation challenging. It is often assumed that a calibration CIR, that is, a measurement from when no person is present, is easily subtracted from a newly captured CIR. We show this is often not the case. We propose modeling the difference between a current set of CIRs and a set of calibration CIRs as a hidden Markov model (HMM). Multiple experimental deployments are performed to collect CIR data and test the performance of this model and compare its performance to existing methods. Our experimental results show an RMSE of 2.85 ns and 2.76 ns for our HMM-based approach, compared to a thresholding method which, if the ideal threshold is known *a priori*, achieves 3.28 ns and 4.58 ns. By using the Baum–Welch algorithm, the HMM-based estimator is shown to be very robust to initial parameter settings. Localization performance is also improved using the HMM-based bistatic delay estimates.[1]

2.1 Introduction

A useful application of UWB impulse radio is detection and tracking of people[2] in buildings. In particular, bistatic and multistatic radar systems are used for this application

[1]

[2]In this paper, we use "people" or "person" to indicate the object being tracked.

[18]. This is done by capturing the CIR, $h(t)$, between transmitter/receiver pairs and detecting changes to the CIR.

This paper describes a contribution to bistatic delay (or equivalently, bistatic range) estimation. A person induces changes in the CIR starting at the bistatic delay, that is, the earliest time delay at which changes occur in the CIR due to the person being tracked. If the bistatic delay is denoted τ_*, then the bistatic range is simply the distance this multipath component has traveled (*i.e.*, $\tau_* c$ where c is the speed of light). If RF energy traveled from the transmitter to the person and then to the receiver, with no additional scattering, then the bistatic range defines an ellipse on which the person is located. Thus bistatic range estimation is a key primitive of UWB tracking systems.

The primary contribution of this work is to develop a method which considers the changes which occur in a CIR at all time delays in order to estimate bistatic delay. Current published research, as described in Section 2.1.1, generally are *first threshold-crossing* methods, that is, they estimate the bistatic delay as the first delay in which a metric exceeds a threshold. As a result, they are (a) sensitive to noise in the CIR prior to the true bistatic delay, and (b) sensitive to the correct setting of the threshold parameter.

Our proposed method uses a HMM to model the changes to the CIR as a function of time delay. The Markov chain is a progression between two states: $X = 0$, meaning that a person in the environment is not causing changes at the current time delay, or $X = 1$, meaning that a person is causing changes at the current time delay. The state of the system is observable only indirectly via the CIR because of noise and the variability in the multipath channel. The distribution of the observations is dependent on the current state of the system, thus the system is a HMM. Using the observations and the system model, the forward-backward algorithm solves for the most likely state at any given time. The bistatic delay estimate is the time delay at which the system transitions from state 0 to state 1.

When solving for the bistatic delay, our proposed method considers all of the available data and, as we show, the error in bistatic delay estimation is reduced compared to the best thresholding scheme. Further, using a Baum–Welch algorithm, we avoid the requirement of knowing *a priori* the correct parameters.

2.1.1 Related Work

Generally, methods to estimate the bistatic delay or range first perform "background subtraction." This means that a prior measurement, or an average of many prior measurements, of the CIR is subtracted from any current CIR measurement. These prior measurements are presumed to be made when the area is empty (*i.e.*, with a static background).

Some work in UWB-based impulse response radar assumes that background subtraction is completely effective in removing the response due to the static environment [12]–[15]. Some work additionally assumes that, after background subtraction, each single multipath component caused by a person's presence can be distinguished perfectly from the impulses caused by other people and the environment [13], [14]. In this paper, we show that ranging can still be performed when these assumptions are not true, as is often the case in a cluttered multipath environment.

One way to estimate the bistatic delay is first to perform "background subtraction," and then to threshold on the amplitude of the difference. Zetik *et al.* [15] describe a thresholding method that uses a simple formula for choosing an appropriate threshold value for accurate range estimation after background subtraction has been performed. Each UWB module has one transmitting and two receiving directional antennas, all relatively close to one another. This makes each UWB module approach a monostatic radar configuration. All of the sensor nodes were pointed inward toward an empty room using directional horn antennas for their experiments. In contrast, our measurements are performed in furnished office environments, and the additional clutter can make background subtraction less effective. The estimation methods described in [15] will be used in this work for comparison.

Another way to estimate the delay is to perform a cross correlation of the received signal with a known target scattering profile and then to threshold the correlation values. Chang *et al.* approach detection by modeling a human body's scattering as a spectral multipath model and cross correlating this model with the received CIRs [19], [20]. Detection is then performed using an adaptive threshold on the cross correlation. In their work they used a UWB radio similar to those used in this work but in a monostatic radar configuration. The human body spectral multipath model was obtained using empirically collected data from their UWB radio. They collected data of a moving human subject in an open field where there was little or no multipath propagation to validate their detection method [19]. They expanded the method to tracking a human target and tested it using additional data collected from the UWB radio [20]. The experimental data for tracking was also collected in an open field. In contrast, we use measured data from cluttered environments to show that our method is robust to the indoor multipath channel.

The work done by Giorgetti and Chiani offers a method of performing time-of-arrival estimation in UWB signals without performing thresholding on the signal [21]. They describe a "non-linear excision filter" to remove binned data that is purely noise to leave only noise-plus-data bins. They use information theoretic criteria to arrive at an estimator.

They offer simulation results using the 802.15.4a channel models. It is unknown how these models change with the presence of a person. The tests performed in this work depend on the presence of a person to affect the channel.

Our work is not the first to propose using HMMs for tracking, however, it is the first, to our knowledge, to propose using a HMM for UWB impulse radar bistatic delay estimation. Nijsure *et al.* used a HMM to model movement in a UWB radar-based tracking system and simulated its performance [22]. In their work, the states of the model are nonoverlapping geographic regions near the radios rather than changes to the received signal. The measurements in [22] are unambiguous power delay profiles. In contrast, our HMM is used to estimate the bistatic range, with only two states, whether or not the CIR is impacted by a person at a given time delay or not. Two-state HMMs have been used in other applications, for example in detecting channel use in dynamic spectrum access [23]. The work in [23] simulated channel access by primary users and the performance of detection by secondary users, who would use the channel opportunistically, using a HMM-based estimator to detect whether a primary user is currently transmitting. Simulations showed improved detection performance for the HMM-based method compared to a threshold-based method.

2.1.2 Organization

This paper is organized as follows. Section 2.2 describes the methods proposed in this work to estimate τ_* using hidden Markov models. Section 2.3 describes the data collection campaigns carried out to test the proposed methods empirically. Results for our proposed methods as well as those from performing simple thresholding and the thresholding method described in [15] are reported in Section 2.4. Finally, conclusions are discussed in Section 2.6.

2.2 Methods

2.2.1 Measurements

Assume that an UWB transmitter sends pulse $\delta(t)$. Due to multipath propagation, the received signal is described by

$$h(t) = \sum_i \alpha_i \delta(t - \tau_i), \tag{2.1}$$

where α_i and τ_i are the complex amplitude and time delay of the ith path, respectively. The line of sight path delay is τ_0. The receiver radio approximately measures the channel

impulse response convolved with the pulse shape. Fig. 2.1(a) is an example of how the transmitted pulse may follow many different paths to arrive at the receiver.

The number of multipath components seen by the receiver depends on the environment around the radios. When a person enters the environment, the person's body will cause a new multipath component at the receiver as well as affect existing multipath components. This is illustrated in Fig. 2.1(b). The delay associated with this new multipath component is τ_*, which we refer to as the *bistatic delay*. The person also affects many α_i for $\tau_i \geq \tau_*$.

In bistatic or multistatic radar systems, the bistatic delay, described by τ_*, is used to locate and track objects near the radio transmitters and receivers. Assuming component i is a single-bounce path (*i.e.*, the path is affected by only one scatter as it travels from transmitter, to the target, and then to the receiver), the scatter is located on an ellipse with foci at the transmitter and receiver locations. That is, the locations where the scatter may be located are points S where the distances from S to the transmitter and receiver, S_t and S_r, sum to:

$$S_t + S_r = c \cdot \tau_i, \tag{2.2}$$

where c is the speed of light.

This work seeks to accurately estimate the bistatic delay τ_*, that of the path created by the person, particularly in environments with "cluttered" impulse responses (*i.e.*, those where individual multipath components arrive closely in time and become difficult to separate from the CIR). Estimation of τ_* is a key primitive operation for UWB impulse radar systems—estimates from multiple transmitter and receiver pairs can be used to determine possible scatter locations under a single-bounce assumption, as we explore in Section 2.2.8.

The IEEE 802.15.4a channel modeling subgroup performed a large measurement campaign to help develop an ultra-wideband channel model for many indoor and outdoor environments [24]. These models are useful for estimating the line-of-sight time of arrival for UWB pulses. They are not useful, however, for simulating the channel impulse response of the environment with the presence of a person or with respect to the person's location within the environment. Estimating τ_* under these channel models in simulation would not be possible without additional models of how the channel is affected as a function of a person's location.

As described in Section 2.1.1, background subtraction is a standard method for removing the static background CIR from a current CIR measurement. However, we have found that background subtraction is not effective in cluttered environments. An example is shown

in Fig. 2.2, which shows the true bistatic delay τ_* and a captured CIR subtracted from a calibration CIR over about 20 ns of time. Both CIRs were averaged over ten measurements, each set of ten captured with a signal-to-noise ratio (SNR) of 31 dB. Individual multipath components are indistinguishable and the signal is very noisy. If background subtraction were effective, the amplitudes prior to τ_* would be significantly lower than the amplitudes after τ_*, however, this is not the case. Better methods than simple subtraction to quantify the changes in the CIR are needed.

2.2.2 Quantification of Change

We describe in this section an alternative to background subtraction. We introduce a divergence measure which quantifies the change between the signal energy measured during the period when the environment is static and the current period.

We consider a discrete-sampled version of the signal energy, r_k, given by

$$r_k = \int_{(k-1/2)T}^{(k+1/2)T} |h(t)|^2 dt, \tag{2.3}$$

where T is the sampling period. For example, in our experimental work, we use $T = 1$ ns which covers between 62 and 63 discrete samples for the CIRs captured using the UWB radios. Essentially, r_k is the energy in multipath components contained within a T-duration window near time delay kT. We call this T duration window "range-bin k." The vector $\mathbf{r} = [r_1, \ldots, r_n]^T$ is the sequence of r_k samples. The unit of time k describes the "fast time" of the radar signal. We choose to estimate the energy in each range-bin rather than using deconvolution to find the CIR. Performing deconvolution to determine the number and arrival times of mulitpaths arriving at the receiver will give incorrect multipath quantities and delays when the multipath experience frequency distortion, which is common for UWB signals [25]. Moreover, the memory and computational burdens are reduced by considering T duration windows rather than all samples.

In this work we use the Kullback–Leibler (KL) divergence to quantify the change in the signal energy r_k at each time k. The KL divergence is a measure of how many additional bits would be required to encode the samples of one distribution relative to another distribution. This is also known as relative entropy [26].

For continuous distributions the asymmetric KL divergence is defined as

$$D(p(x)\|q(x)) = \int p(x) \log \frac{p(x)}{q(x)} dx, \tag{2.4}$$

where $p(x)$ and $q(x)$ are the probability densities of r_k for the calibration measurements and for those under test, respectively. These measurements are with respect to the "slow time" of the captured CIRs. The symmetric KL divergence is defined as $D(p(x)\|q(x)) + D(q(x)\|p(x))$.

The observation signal, O_k, in this model represents the difference between r_k and r_k of the empty room, that is, the calibration samples. In this work, this difference was calculated as the symmetric KL divergence.

For the observed signal, O_k, we use the symmetric KL divergence assuming Gaussian distributions for r_k. This measure is given in closed form by,

$$O_k = \frac{1}{2}\left(\frac{\sigma_p^2}{\sigma_q^2} + \frac{\sigma_q^2}{\sigma_p^2} + \frac{(\mu_p - \mu_q)^2\left(\sigma_p^2 + \sigma_q^2\right)}{\sigma_p^2\sigma_q^2}\right) - 1, \tag{2.5}$$

where μ_p and σ_p^2 are the mean and variance of r_k during calibration, and μ_q and σ_q^2 are the mean and variance of r_k from the CIR measurements collected for testing. These mean and variance estimates are for a fixed k over several CIRs, which is the "slow time." This closed form solution for O_k is non-negative and the pdf $f_{O,i}$ will allow us to estimate X_k by applying our hidden Markov model. The unit of measurement for the KL divergence, or O_k, is bits.

The assumption that r_k is Gaussian with respect to the "slow time" of the measurements is important to the closed form solution of O_k given in equation 2.5. To show that r_k follows a Gaussian distribution, each set of 10 samples of r_k for the empty room was normalized to have a mean of 0 and a variance of 1. The SNR for these empty room measurements was 31 dB. These samples were then aggregated for testing. With 10 sets of 90 samples of r_k for the six radio pairs gives 5400 samples. To reduce sampling instability, each CIR was interpolated by a factor of four and then cross correlated with each other to align them in time. A histogram of the normalized samples is given in Fig 2.3. Submitting these samples to a Kolmogorov–Smirnov test fails to reject the null hypothesis that they come from a standard normal distribution with $p = 0.198$. These results are similar for other CIRs captured throughout this experiment.

An example of an observation vector $\mathbf{O}$ of KL divergences is given in Fig. 2.4. This particular example is one where a first threshold-crossing method would be unable to correctly estimate the true bistatic delay, k_* where $k_* = \lfloor \frac{\tau_*}{T} \rfloor$, of 15. For this particular set of empty-room and target CIRs, the SNRs were, respectively, 27 and 28 dB. This example shows how the assumption of easily being able to discern the background signal from the

changes to the CIR can sometimes be wrong. In this case, there is a very large divergence at a time when the signals should have shown little difference. The majority of observation vectors will not exhibit this behavior but the errors of vectors such as these significantly impact the overall error for an environment as will be shown in Section 2.4.

Other distance measures or distributions could be applied. However, the KL-divergence and Gaussian assumption provide a standard approach for this proof-of-concept study.

2.2.3 CIR Changes as a Hidden Markov Model

A hidden Markov model is a special case of a Markov chain. The states of a HMM are not directly observable but may be inferred. Other signals available for observation help determine the past and current states of the system. Let π_i be the probability of initially starting the HMM in state i, P_{ij} is the probability of transitioning from state i to state j, and $f_{O,i}$ is the probability of observing signal O given the HMM is in state i, that is, $f(O|X_k = i)$. A simple illustration of a hidden Markov model is shown in Fig. 2.5.

In the case when the observations are continuous, we use the probability density function (pdf) conditioned on the state, $f_{O,i}$, for a continuous valued random variable. This is the typical way to describe a HMM for continuous-valued observations [27].

By knowing $f_{O,i}$, P_{ij}, and π_i, a best estimate of the current state at each time, $\hat{X}_k$, can be calculated. This is found by applying the forward-backward algorithm to the sequence of observation signals. When the estimated states transition from $\hat{X}_k = 0$ to $\hat{X}_{k+1} = 1$, this gives an estimate for k_* and indicates the presence of a person due to the changes to the observation vector.

Estimation of k_*, where $k_* = \lfloor \frac{\tau_*}{T} \rfloor$, is equivalent to estimating τ_*. Due to multipath scattering and the person's impact on those later-arriving signals, r_k will experience changes, or $X_k = 1$, for many $k \geq k_*$. The advantage of applying a HMM is that information over all k is considered when solving for X_k rather than considering values at each k independently of changes at all other k.

A more thorough introduction to hidden Markov models and the algorithms used to infer information about them can be found in [27].

2.2.4 Continuous Observation Densities

The observations O_k are continuous valued and their probability distribution is described by $f_{O,i}$, the probability density function of O_k given $X_k = i$, $i \in \{0, 1\}$. The HMM parameters $f_{O,i}$, π_i, and P_{ij} are estimated using the data $\mathcal{D}$ collected in one room and are used as initial estimates of the HMM parameters when estimating k_* for the other room.

The data sets $\mathcal{D}_i$, for each state i, are made using the knowledge of k_* by

$$\mathcal{D}_0 = \{O_k | k < k_*\}, \tag{2.6}$$

$$\mathcal{D}_1 = \{O_k | k \geq k_*\}. \tag{2.7}$$

Dividing the observation signals in this way assumes that there will only be one transition from state 0 to state 1 and no transitions back to state 0, that is $P_{10} = 0$ and $P_{11} = 1$.

Under the assumption that $X_k = 1$ given $k \geq k_*$, one may also assume that $P_{1,0} = 0$ and $P_{1,1} = 1$, that is, $P(O_k | X_k = 1)$ remains constant as k increases. This assumption may not be true—a person's effect will eventually diminish for large k. Also, a probability of 0 leaves little opportunity for change during optimization. To improve the model, we allow a small probability of returning from state 1 to state 0 (*i.e.*, set $P_{10} = \epsilon$ where ϵ is a small value greater than 0).

In [16], no assumptions were made regarding the distribution the observations took on. The distribution was estimated by performing an Expectation Maximization algorithm to fit the data to a Gaussian mixture model. This operation was computationally expensive but effective. In this work we utilize our observation that the densities are similar to a log-normal distribution. Under this assumption, well known maximum-likelihood estimates are used for the distribution parameters. Fig. 2.6 shows the empirical cumulative distribution functions (CDFs) of the aggregate samples before and after k_* for one room. The natural log is applied to O_k in these distributions. This log-normal approximation reduces the computational load without sacrificing solving accuracy.

Initial estimates for π_i and P_{ij} are given by [27, eq. (40a–b)] using the training data.

2.2.5 HMM Solving

The HMM parameters are described by λ as

$$\lambda = [\pi_i, P_{ij}, f_{O,i}]\,. \tag{2.8}$$

The data from one room is used as training data to obtain an initial estimate of λ to begin solving for k_* with the other room's data, or that of the measurement room. The following describes how k_* is estimated for the measurement room once λ is estimated from the training data, as described previously.

Finding $\hat{X}_k$, the estimate of X_k, for the measurement room is done by solving the forward-backward algorithm. This algorithm finds the most likely state X at each range-bin k [27].

$$\hat{X}_k = \arg\max_i P(X_k = i|\mathbf{O}, \lambda). \tag{2.9}$$

The forward-backward algorithm is different than the Viterbi algorithm, which finds the most likely state sequence over all k. It may seem more appropriate to use the Viterbi algorithm to estimate when the state change occurs. The Viterbi algorithm, however, only returns a state sequence. By using the forward-backward algorithm, the additional uncertainty information of $P(X_k = i|\mathbf{O}, \lambda)$ is available for each k when performing localization. It should be noted that estimates for k_* are not constrained by the room boundaries or by any prior information about where the person might be located.

After estimates for X_k are obtained, the Baum–Welch algorithm uses these estimates to update the set of HMM parameters such that

$$P(\mathbf{O}|i, \lambda_{n+1}) > P(\mathbf{O}|i, \lambda_n). \tag{2.10}$$

This algorithm is an iterative optimization on the space of λ to maximize $P(\mathbf{O}|i, \lambda_n)$.

The HMM parameters are updated over all sets of $\mathcal{D}$ as described by Rabiner [27]. Also, $f_{O,i}$ is again found by estimating the distribution as log-normal using $\mathcal{D}_i$. However, $\mathcal{D}_i$ is now found as

$$\mathcal{D}_i = \{O_k|\hat{X}_k = i\}. \tag{2.11}$$

The algorithm continues for a predetermined number of iterations or until $P(\mathbf{O}|\lambda_n)$ no longer increases more than a given tolerance with each iteration, that is, $P(\mathbf{O}|\lambda_n) - P(\mathbf{O}|\lambda_{n-1}) < \epsilon$. The final estimate for k_* is

$$\hat{k}_* = \{k_*|\hat{X}_k \neq 1 \forall k < k_*\}. \tag{2.12}$$

This finds a local maximum in the space of possible λ but may not find the global maximum. The effectiveness of this algorithm is dependent on the initial values of the HMM parameters and the data itself. Other optimization algorithms exist but were not explored in this research.

2.2.6 First Threshold Crossing

A standard method to determine the bistatic delay, k_*, is simply to find the first time at which O_k is greater than a threshold. We refer to this method as *first threshold crossing* (FTC). Specifically the estimate of k_* in first threshold crossing is given by

$$\hat{k}_*^{FTC} = \arg\min_k O_k > \gamma, \tag{2.13}$$

where γ is a threshold. We show the performance of this method in Fig. 2.7 as a function of γ. To show how the method would perform with training, we assume that γ is set by using the γ that achieves the lowest root mean squared error (RMSE) in one room, and test performance with that γ in the other room.

The work presented by Zetik *et al.* in [15] gives another method for thresholding the received CIR to estimate τ_*. This method is also used for comparison in Section 2.4.1.

2.2.7 Localization

Multiple range estimates allow localization to be performed. In this section, we describe methods for merging bistatic range estimates to obtain a position estimate. Clearly, range estimates contain errors, and any location estimator must deal with these noisy inputs. The works of Paolini *et al.* [28] and Bartoletti *et al.* [29] provide important information about uncertainty and error in performing localization in an UWB network.

One advantage of the HMM-based approach we propose in this paper is that it provides a "soft" decision on the bistatic range estimate. The forward-backward algorithm quantifies the probability of each state i at each time index k, $P(X_k = i|\mathbf{O}, \lambda)$. If the conditional probability of state 1 increases from zero to one very quickly at time k, then this delay bin k is very likely to have been the true bistatic delay. If the conditional probability increases slowly from zero to one over several delay bins, then it becomes more difficult to estimate k_* over those bins when the probability increases. Essentially, a quantification of the probability of each delay bin k being the true bistatic delay is given by the rate at which the conditional probability changes.

The forward-backward algorithm finds the conditional probability of being in a given state at time k. To simplify notation going forward, we will let $\alpha_k = P(X_k = 1|\mathbf{O}, \lambda)$. Since there are only two states, α_k fully describes the probability of being in a given state at time k. Also, let $(x)^+$ be defined by

$$(x)^+ = \begin{cases} x & \text{if } x \geq 0 \\ 0 & \text{if } x < 0. \end{cases} \tag{2.14}$$

Assuming a single-bounce model, each time delay measurement corresponds to a region on the plane given an ellipsoid with the transmitting and receiving radios at the foci. For a location estimate on a 2D plane, at least three radio pairs must give range estimates for the overlapping elliptical regions to produce a unique solution, assuming noise-free range estimates. Due to the cluttered environment, whose background UWB reflections are often much stronger than the ones caused by a person, the range estimates cannot be assumed to be noise-free. For this work, to mitigate the effect of having range estimate inaccuracy, we obtained data from six radio pairs.

One way localization can be solved is as an inverse problem, described by Chang *et al.* as a semilinear algorithm (SLA) [13] which models the radio locations and range estimates as a linear function [13, eq. (4)]. SLA is solved using a linear least squares method. Where range estimates alone are available, solving the problem as an inverse problem makes the most sense since these estimates will often not converge perfectly due to errors and noise.

The output of the HMM, however, is more than a simple range estimate. Additional information about the probability of being in one of the two HMM states is available. This additional uncertainty at each time k can be used to improve localization accuracy.

The work of Ergut *et al.* [30] offers another localization method complementary to the range estimation method proposed in this work. They propose an artificial neural network to localize a target within a sensor network which returns range estimates as inputs to the neural network. Their localization method, however, requires localization training and makes the assumption of high SNR range estimates. The work also fails to show how their method performs using empirically measured channel impulse responses.

The work of Chiani *et al.* performs localization using a *soft image* derived from the time-of-arrival estimates [31]. This is similar to our proposed localization method in that no single range estimate is used to perform localization but an intermediate set of data, which in our case is the output of the forward-backward algorithm. No detection methods will be applied, however, to the UWB image. Chiani *et al.* also offer a number of ways to obtain pixel values for the *soft image*.

By nature of the experiments performed, tracking algorithms were not applied. The work of Bartoletti *et al.* apply tracking algorithms that may aid in the localization of a moving person [32].

2.2.8 Proposed Localization Method

In this work, localization is solved as a forward problem as follows. We discretize space into P pixels containing the area being monitored. We denote l_i to be a quantification of the "presence" of a person in pixel i. The image vector is then

$$L = [l_1, \ldots, l_P]^T, \tag{2.15}$$

where pixel i is centered at coordinate $z_i = (x_i, y_i)$. A person in pixel i would, assuming the single-bounce model, be measured to be in range-bin k_i^m for transmitter/receiver pair m, where $m \in \{1, \ldots, M\}$,

$$k_i^m = \left\lceil \frac{\|t_m - z_i\| + \|z_i - r_m\| - \|t_m - r_m\|}{d_k} \right\rceil, \tag{2.16}$$

where t_m and r_m are the transmitter and receiver coordinates for link m and d_k is the distance light travels during one time bin. The value l_i is given by

$$l_i = \left[\sum_{m=1}^{M} [A^m]_i^p \right]^{\frac{1}{p}}, \tag{2.17}$$

where A is the non-negative difference function of α at k_i^m,

$$[A^m]_i = (\alpha_{k_i^m} - \alpha_{k_i^m - 1})^+, \tag{2.18}$$

with $\alpha_0 = 0$. Equation (2.17) is the p-norm of $\{A^m\}$ for all radio pairs $m = 1, \ldots, M$ at pixel i. A p-norm of 0 (*i.e.*, $p = 0$) gives a count of nonzero values and a p-norm of 1 is a sum of the elements. In this work, $p = 0.2$ was found to give the best performance and was the value used for the results given in Section 2.4.2. This p-value weights the elements of A such that, qualitatively, lower values are weighted more and higher values are weighted less.

Rather than using α_k, localization can also be done using estimates $\hat{k}_*$. This would change the way A is calculated from what is given in Equation (2.18) to:

$$[A^m]_i = \begin{cases} 1 & \text{if } i = \hat{k}_* \\ 0 & \text{otherwise.} \end{cases} \tag{2.19}$$

Results for both of these methods for solving localization as a forward problem as well as solving using SLA are given in Section 2.4.5.

To understand pixel value l_i more intuitively, we recall that $\alpha_{k_i^m} - \alpha_{k_i^m - 1}$ is a soft metric for the probability that pixel i is at the same bistatic range as the person, as indicated by the measurement on link m. Due to the p-norm in (2.17), l_i is a type of average of these probabilities over all links. This method is especially useful when the measurements from a link are ambiguous, and thus α_k for that link doesn't change from zero to one suddenly. The uncertainty in $\{\alpha_k\}_k$ is reflected in the presence image L.

For purposes of noise reduction, we apply a 2-D Gaussian filter to image L. For experiments with one person in the area, we take the coordinate of the pixel with highest l_i (after the filtering) as the location of the person.

2.3 Experiment

We conduct two types of experiments for evaluation of our proposed algorithms. First, we conduct in-room experiments where transmitters and receivers are in the same room as the person being located. Second, we conduct an experiment in which the transmitter and receiver are on the other side of an interior wall of the room in which the person is located. In all experiments, we use two P220 UWB impulse radios from Time Domain, Inc., to capture CIR measurements with an antenna height of 0.9 m. The radios transmitted at power level of -16.13 dBm with a transmitted center frequency of 4.7 GHz and a 10 dB radiated bandwidth of 3.2 GHz. Pulses are transmitted at an average rate of 9.6 million pulses per second. Additional information about the P220 radios can be obtained from Time Domain [33].

2.3.1 In-room Experiments

We first conduct measurements in rooms 3325 and 1280 in the Merrill Engineering Building. Two rooms are measured so that one room can be used as a training room while the other is used as an experiment room. Figs. 2.8(a) and 2.8(b) describe the positions of the radios and where the person stands in each room. Room 3325 contains typical office furniture; desks, chairs, bookshelves, and computers. It measures 6.2 m by 6.2 m with the ceiling 2.5 m from the floor. Room 1280 is a classroom and all of the desks and furnishings were removed from the room for the experiment. Room 1280 measures 8 m by 8.2 m with the ceiling 2.7 m from the floor.

We collect both empty-room (*i.e.*, no person in the room) calibration measurements and measurements which represent all measurements possible in a four UWB transceiver

multistatic network when a person is standing at any of the possible grid points in the two rooms. Since we have only two UWB transceivers, we conduct these measurements as follows.

The two radios are placed in any of the four locations designated for the radios in the room. Ten calibration measurements of the CIR, or r_k, are taken when the room is empty. Then, at each of the designated points, a person stands and remains as motionless as possible while ten more measurements of the CIR are taken. Each set of ten measurements was captured over approximately five seconds. After collecting measurements at all points, the two radios are moved. This process is repeated for the $M = 6$ pair-wise radio locations. The full process is repeated in the second room. These sets of ten are those used to estimate μ and σ^2 for r_k for the calibration and measurement sets.

Experiment A uses the data collected in room 1208 as the training room data and the data collected in room 3325 as the data for the experiment room. Experiment B swaps the data used for the training and experiment rooms and performs the estimation again.

2.3.2 Through-wall Experiment

In addition to ranging and localizing a person that is in the same room as the radios, one data set is also collected to test ranging through an interior wall. Two radios are placed 1 m apart from one another and 18 cm from the wall in room 3220 separating it from room 3230 in the Merrill Engineering Building at the University of Utah. Room 3220 and 3230 both measure 6.7 m by 4.9 m with a ceiling height of 2.7 m. The separating wall is approximately 10 cm thick and is constructed of a metal support with internal insulating material and covered in drywall.

We also report the power loss due to wall penetration, in order to characterize the experiment condition. To estimate the penetration loss of the wall, the CIR is measured with the radios 4.5 m apart with both radios in room 3220. The transmitting radio is then placed on the other side of the wall in room 3230, and the receiving radio is also moved to maintain a 4.5 m separation. The CIR is measured again and the line-of-sight component of two measured CIRs are compared. The measured power loss of the wall is approximately 5 dB over the 3–5 GHz band.

The measurements are made as follows. A person stands at 30 different locations in the adjacent room 3230 while the CIR was captured 20 times per location. Fig. 2.9 shows these two rooms with their corresponding person and radio locations. Both before and after all of these CIRs are sampled with a person present, the CIR for the empty room is captured 100 times. UWB pulse integration is also increased by a factor of 8 from what was used

in the other experiments. This increases the SNR of each CIR at the cost of lowering the maximum possible sampling rate.

This through wall experiment is performed for just one radio pair, which is insufficient for localization. Instead, the purpose of this through-wall experiment is to allow us to quantify the performance of UWB impulse radio bistatic delay estimation.

2.4 Results

In this section, we apply the methods proposed in Section 2.2 to the data collected as described in Section 2.3. We measure the performance of our proposed HMM-based bistatic delay estimator in three ways: (1) the RMSE of the bistatic delay estimator, (2) the false negative and false positive rates, and (3) the performance of localization using our bistatic delay estimates. We compare the results of our method of estimating bistatic delay to simple thresholding as well as the thresholding method given in [15].

The bistatic delay error is the difference between the person's actual bistatic delay and the estimated bistatic delay,

$$\varepsilon = T \left| \hat{k}_* - k_* \right| . \tag{2.20}$$

We use RMSE across all experiments to quantify average performance.

We report false negative and false positive rates for the methods studied. For bistatic delay estimation, a false negative is when there was no person's bistatic delay detected when a person is actually present. For our HMM-based method, this corresponds to the forward-backward algorithm detecting no transition from state 0 to state 1 for the measured CIR. A false positive is when there was a bistatic delay estimated when no person was present.

In all results, we chose a delay-bin duration T of 1 ns. The choice of T is a trade-off between computational requirements and quantization noise. We note that 1 ns of time corresponds to about 30 cm of distance traveled at the speed of light, approximately the width of an adult human body. Further, our results show errors significantly higher than 1 ns, and thus it has not been necessary for us to reduce T further.

2.4.1 First Threshold Crossing

First, we test the performance of the FTC estimator as described in Section 2.2.6. We find the threshold that is optimal (for minimum RMSE) for the training room and then use that threshold in the testing room. From this method, a minimum RMSE of 5.25 ns

is achieved for Experiment A and 5.20 ns for Experiment B. Next, we see what minimum could have been obtained for the testing room even if the optimal threshold for that room had been known. These absolute minimums achieved are 3.28 ns and 4.58 ns, respectively. Fig 2.7 shows how the RMSE varies as a function of the threshold. Clearly, the optimal threshold would not be known *a priori* for each room. Fig. 2.7 shows the sensitivity of the RMSE to the chosen threshold. For Experiment A there is a large change in the estimates with a small change to γ. This large change to the RMSE, occurring near γ values of 65 and 99 bits, are due primarily to one set of CIRs for one point and radio pair. Without knowledge of the true values for k_*, one would still notice the large change to $\hat{k}_*$ with small changes to γ. The effect on RMSE due to this one particular person-location and radio-pair combination, which we also describe as an outlier, is shown in Fig. 2.10.

There were no false negatives for the range of γ tested in Fig 2.7 for either experiment using the first threshold crossing method.

The work done by Zetik *et al.* [15] gives a somewhat different method for thresholding the signals. The background is continually updated for each UWB node, which would correspond to a radio pair in our work, as:

$$\mathbf{b}^i = \alpha \mathbf{b}^{i-1} + (1-\alpha)\mathbf{m}^i, \tag{2.21}$$

where $\mathbf{b}$ is the background estimate and $\mathbf{m}$ is the newly measured CIR. The signal $\mathbf{s}$ then used for thresholding is:

$$\mathbf{s}^i = \mathbf{m}^i - \mathbf{b}^i. \tag{2.22}$$

This removes the static background signal from the time-varying signal, which is what we wish to detect and range.

The threshold is calculated as:

$$t^i = \left(0.3 + 0.7\frac{n^i}{||\mathbf{s}^i||_\infty}\right)||\mathbf{s}^i||_\infty, \tag{2.23}$$

where n^i is the peak noise level of m^i.

Using the method of [15], described in Equations (2.21), (2.22), and (2.23), and the data collected, we obtain an RMSE of 6.5 ns and 10.6 ns for experiments A and B, respectively.

When first threshold crossing is performed on the through-wall experiment data, a plot of RMSE versus threshold is obtained and shown in Fig. 2.11. This is comparable to

those shown in Fig. 2.7. Notice that the γ that achieves the optimal estimation of k_* is different for each experiment and varies significantly. In other words, the optimal γ cannot be determined from data measured in a different location.

2.4.2 HMM-based Method

The HMM and process described in Section 2.2.5 are applied to the two in-room experimental data sets. The changes to RMSE for each iteration of the Baum–Welch algorithm is shown in Fig 2.12. The RMSE achieved after 15 iterations is 2.85 ns and 2.76 ns for Experiments A and B, respectively. This corresponds to less than 90 cm of range error. Others have described how range error corresponds to localization error in UWB sensor networks [28], [29]. There were no false negatives. The bias, $E[\hat{k}_* - k_*]$, was -0.3 ns for Experiment A and 0.2 ns for Experiment B.

For all points on the line-of-sight of two radios, the estimated range was always $\hat{r}_k = 1\,ns$, which is between times 0 n and 1 n because $T = 1\,ns$, which is the correct estimate. Although the line-of-sight signal is blocked by the person, there is still a significant amount of energy arriving at the receiving radio from diffraction and reflection in the environment. The observations O_k from the received CIRs with the line-of-sight path blocked indicate that $\hat{X}_k = 1$ over all k rather than transitioning from $X_k = 0$ to $X_{k+1} = 1$ at some k, giving an estimated range of $\hat{r}_k = 1\,ns$.

The marked improvement in RMSE from using a HMM over energy detection also comes without foreknowledge of an ideal threshold value. Although an initial estimate for λ is required, the Baum–Welch algorithm eliminates much of the error due to a poor estimate, as will be shown with the through-wall results 2.4.3. The HMM, unlike a simple threshold, takes into account the data across all time values to estimate k_*.

The stopping condition used for the given results is to continue the Baum–Welch algorithm until there is little change to $P(\mathbf{O}|\lambda)$ from one iteration to the next. That is $P(\mathbf{O}|\lambda_n) - P(\mathbf{O}|\lambda_{n-1}) < \epsilon$. Experiment A converges, using this metric, after 9 iterations and Experiment B after 14 iterations.

2.4.3 Through-wall experiment

Our proposed HMM method is also applied to data captured through a wall dividing two rooms as described in Section 2.3.2. Observation vectors are calculated using all of the available empty room CIRs and CIRs with a person present. With the observation vectors and an initial estimate for the HMM parameters λ, estimates for k_* can be found.

Using the λ that is found to be optimum for any one of the three environments as the initial λ for any of the other environments results in the same solution for λ from the Baum–Welch algorithm. This is illustrated using the through wall data. For the through wall data, there are three choices of λ, two obtained from the data collected from the two in-room experiments described in Section 2.3.1 and one from the data and known locations of this through wall data. The λ obtained from the through wall data could not be used in a production system because it is derived using a knowledge of k_*. If k_* is known, there is no reason to use it to find λ to then estimate k_*. It is used here solely for illustrative purposes.

Fig. 2.13 shows the bistatic delay RMSE at each iteration of the Baum–Welch algorithm for the three different choices for λ at the first iteration. The choice of λ greatly influences the RMSE at first, but the effect of the choice is ultimately negated by the Baum–Welch algorithm. The final RMSE in all three cases is 1.33 ns.

This final error is better than the results obtained with the subject in the same room as the radios. There are several reasons for this.

1. *Number of samples*: Many more samples of the empty room were collected and used in determining the KL-divergences in the through-wall experiment (200) compared to the in-room experiments (10). These additional samples help to reduce the noise in the observation vectors. The effect of choosing different empty room samples is explored further below.

2. *Additional integration*: Additional signal integration was done in sampling to reduce noise in the CIRs because of the additional path loss in the through-wall experiment.

To show the effect of the number of empty room samples on the performance of the ranging estimation (item 1 above), we run an experiment in which we reduce the number of empty-room samples used in the through-wall experiment. Here, we calculate observation vectors of KL-divergences using sets of 20 sequential empty room samples. From the two sets of 100 empty room samples, this leads to 162 sets of sequential samples. The initial choice of λ was the same used in Experiment A. The overall RMSE was calculated for each of these sets of empty room samples. Two of the 30 person locations had a wide variation in their range estimate depending on which set of empty room samples was chosen. Fig. 2.14 shows the empirical CDF of the final RMSE obtained using each of these sets of empty room samples both with and without these two person locations.

For the trials using all person locations, 12.3% of the trials resulted in an RMSE better than the 1.33 ns achieved using all of the empty room samples together. The overall RMSE

for all of the trials using 20 empty room samples is 4.19 ns. This illustrates that, on average, using a fewer number of empty room samples degrades performance.

2.4.4 False Positives

Testing for false positives, or nonzero estimates of k_* in empty room samples, was also performed. The Baum–Welch algorithm was not performed on these samples, that is, no updating of the HMM parameters was done for re-estimation of k_*.

False positives were tested by randomly dividing the set of empty-room samples into the known empty-room and possible point sample sets. Due to the limited sample sizes for empty-room samples, this random set division allows us to simulate how false positive tests might perform using different sample sets that are not available. For each radio pair, the available samples were divided evenly between the known empty-room sample set and the possible point sample set. These two sets were used to find the observation vector of KL divergences, which the HMM uses to estimate k_*.

For each of the six transmitter/receiver pairs for each of the two rooms, 1000 trials were performed using the random subset division described for a total of 12 000 trials. Of these a total of 50 trials resulted in false positives, that is, a 4.2×10^{-3} false positive rate. We note that over half of the false positives come from a single transmitter/receiver pair in one of the rooms. Notably, this pair had just 10 empty-room samples available for testing. This is the fewest number of empty-room samples for any transmitter receiver pair.

2.4.5 Localization

Results for localization are given for both the forward method described in Section 2.2.8 and the SLA described described by Chang *et al.* [13]. The forward solving method is done in two ways, first using α_k where $\alpha_k = P(X_k = 1|\mathbf{O}, \lambda)$ and second using only the range estimates, $\hat{k}_*$, without the additional information of the probability of being in a given state.

The SLA described by Chang *et al.* only uses range estimates for localization. A summary of the results of each localization method with its available information is given in Tables 2.1 and 2.2. All values are given in centimeters.

The forward solving method described here gives location estimates that are significantly better than those from the SLA described by Chang *et al.* Taking into account α_k rather than using $\hat{k}_*$ alone also improves the location estimates for the forward solving method.

Figs. 2.15 and 2.16 describe the true person locations, as shown previously in Fig 2.8, and the estimates for those locations using the forward solving method with all available information.

Range estimates from three unique radio pairs is sufficient to unambiguously localize a target. In this work there are estimates from six radios pairs for each localization image. Having information from additional radio pairs aids in accurate localization because some of the estimates may be inaccurate. As long as the information from at least three radio pairs are accurate, the target's location can be accurately estimated. Also, as shown in the results given, using all of the available information from the forward-backward algorithm, and not using the range estimate alone, increases localization accuracy.

Chang *et al.* [13] offer a Cramér–Rao lower bound on location estimation accuracy assuming range estimates are corrupted by Gaussian noise. They find asymptotic bounds as the number of transmitters and receivers grows for a few different scenarios. For an object at the origin, they find the bound to be

$$\frac{2\sigma^2}{NM}, \tag{2.24}$$

where NM is the number of UWB links in the network, which in our case is 6. Range errors of 2.85 ns and 2.76 ns correspond to a σ of 85 cm and 83 cm, respectively. This gives lower bounds of 24 cm and 23 cm for localization error. Notice that in Table 2.1 the results for using only range estimates results in errors of 155 cm and 75 cm, respectively. The actual error is higher than these bounds. This may be due to the fact that the noise in the range estimates may not be Gaussian, as is assumed by Chang *et al.* This may also be because the assumption that range errors are independent on different links may not be valid. Also note that much better performance is achieved when all of the additional information available from the forward-backward algorithm is used rather than using range estimates alone. However, no lower bound on performance is available in this case.

2.5 Discussion

One primary limitation of the algorithm as proposed is that it assumes only one person is causing changes to the CIR. To account for more people, future work must expand the HMM-based estimator to estimate a bistatic delay for each person in the environment. Research must determine what methods to use in the multiple person case. For example, more states could be added to the Markov model that account for more than the channel impulse response simply being affected or not. Additional states could estimate the number of targets to have affected the channel. Another possibility is if joint estimation of the number of people and their bistatic delays improves performance. Once localization of multiple

targets has been performed, several multitarget tracking methods have been developed for RSS-based device free localization [34]–[39].

Another limitation of the proposed algorithm is its reliance on calibration CIRs. We have shown that the proposed method is robust to variances in the initial choice of λ but it is not to significant changes to the environment. New calibration samples would be needed each time a change in the environment requires it. One possible way to eliminate the calibration requirement is to use the CIRs that were sampled immediately preceding the CIRs with a possible target. This, however, may introduce bias and make static targets harder to detect.

2.6 Conclusions

In this paper, we introduce and experimentally verify a hidden Markov model-based algorithm for estimating the bistatic delay in an UWB impulse radar system. We show the proposed algorithm achieves a lower RMSE than first threshold crossing methods for highly cluttered multipath environments. Applying the Baum–Welch algorithm allows the proposed estimator to adapt its parameters to be best for the particular environment. We show the algorithm is robust to initialization parameters derived from a different environment.

Compared to using the first threshold crossing estimate of τ_*, our method reduces error by almost half. Since these estimates of the person's bistatic delay are used directly in tracking algorithms, we expect to similarly improve UWB-based localization performance.

The forward solving method described here for localization using the probabilities α_k was very effective, achieving a median error of 18 cm.

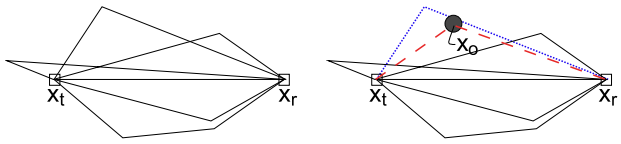

(a) Static Environment (b) Person's Effect

Figure 2.1. When a person appears at x_0 in the environment between the transmitter at x_t and receiver at x_r, an additional path is caused with path length $\|x_t - x_0\| + \|x_0 - x_r\|$, where $\|\cdot\|$ is the L^2 norm, and also affects multipath components with longer path lengths.

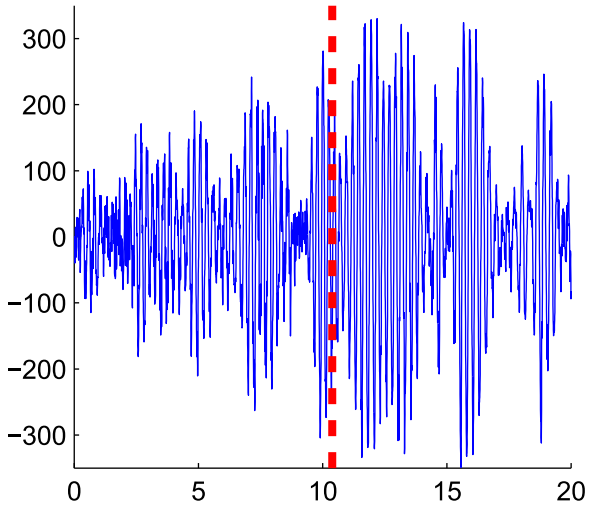

Figure 2.2. The difference between a calibration CIR and a new CIR gives a noisy signal with multipath components that are indistinguishable from one another. The red, dashed line is the actual bistatic delay (*i.e.*, τ_*).

Table 2.1. RMS Localization Error (cm)

	Forward		SLA
	All Info	Range Only	Range Only
Rm 3325	36	155	165
Rm 1208	24	75	194

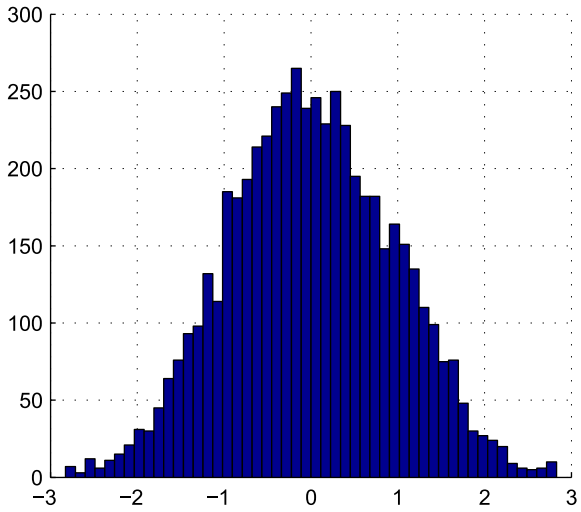

Figure 2.3. Empty room samples normalized to have zero mean and a variance of 1 exhibit a Gaussian distribution.

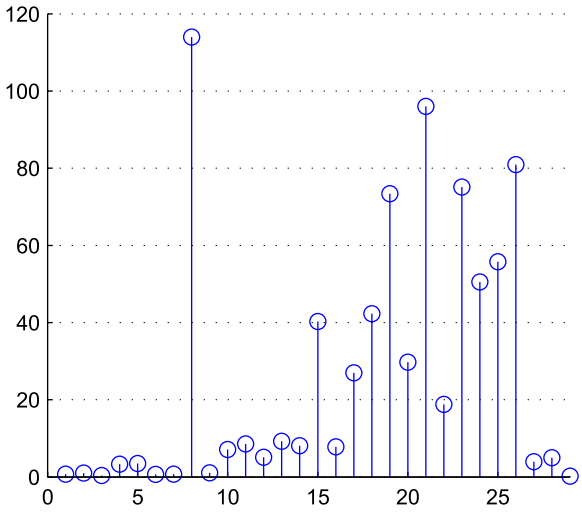

Figure 2.4. An example of an observation vector where no threshold can find the true k_*, which is 15 in this case. The HMM correctly estimated k_* for this vector.

Table 2.2. Median Localization Error (cm)

	Forward		SLA
	All Info	Range Only	Range Only
Rm 3325	16	67	159
Rm 1208	16	29	172

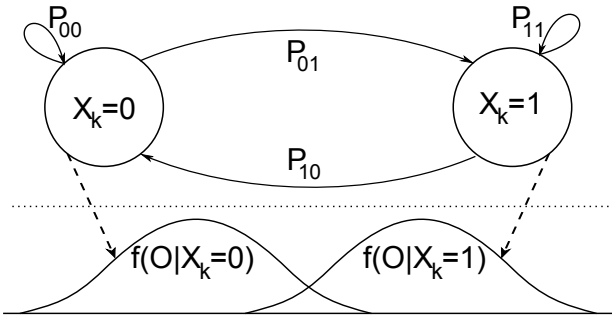

Figure 2.5. The change in CIR measurement we observe at range-bin k, O_k, has a distribution dependent on the state, X_k, of a hidden Markov chain.

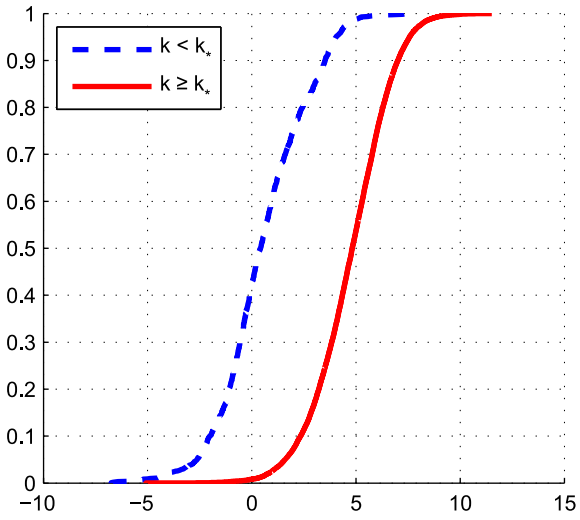

Figure 2.6. Empirical CDFs of the log of O_k for one room. Although these distributions are not precisely log-normal, this assumption is reasonable for the solving methods.

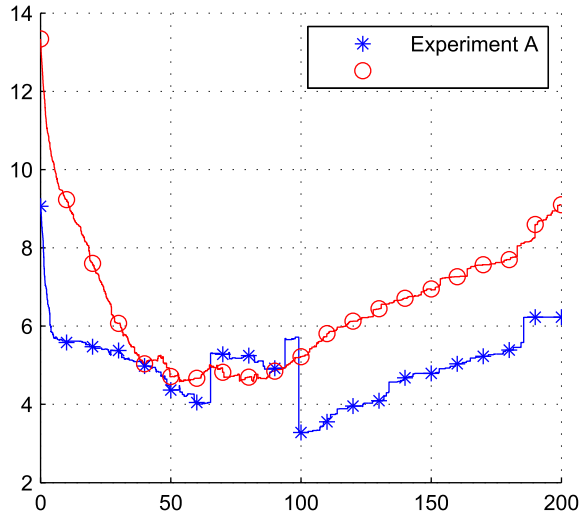

Figure 2.7. Performance of *first threshold crossing* method given by equation (2.13) as a function of threshold γ.

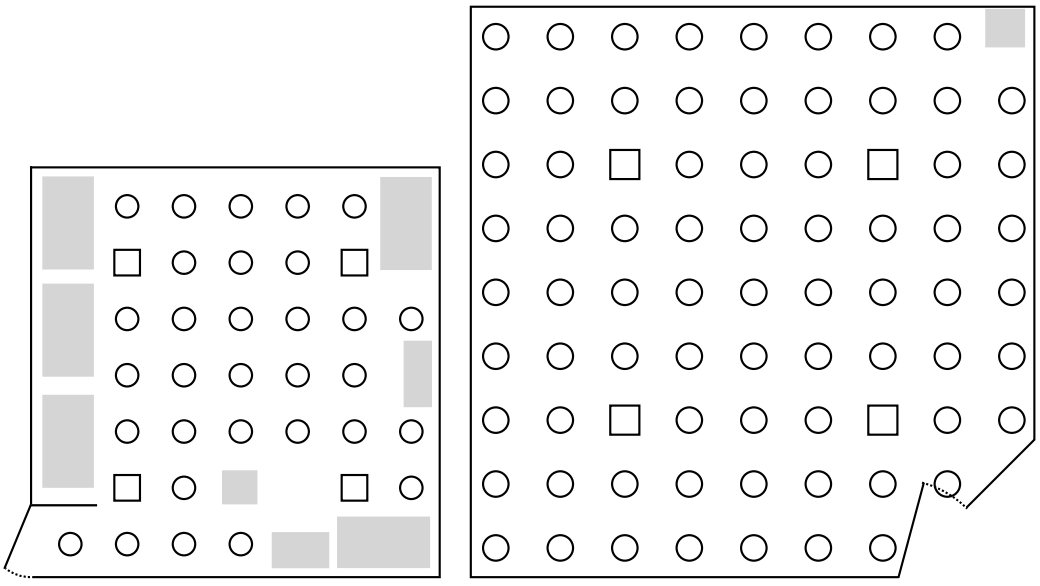

(a) Room 3325 (b) Room 1280

Figure 2.8. Circles are points where the person would stand and squares are radio locations. Gray rectangles are furniture. Neighboring points are spaced 90 cm apart.

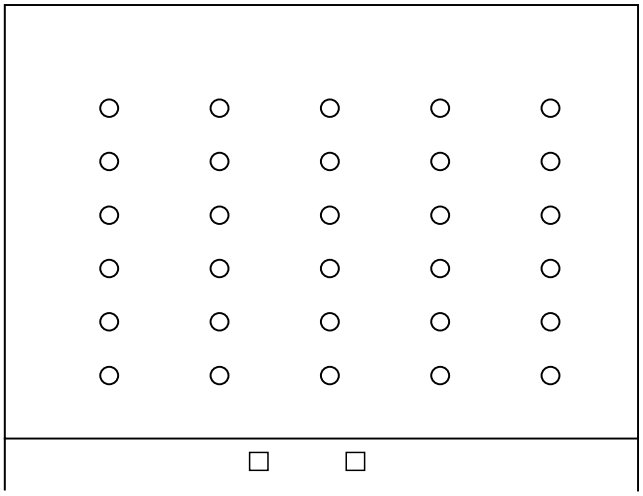

Figure 2.9. Squares represent radio locations in room 3220 and circles represent person locations in room 3230. Person locations are spaced 60 and 120 cm apart.

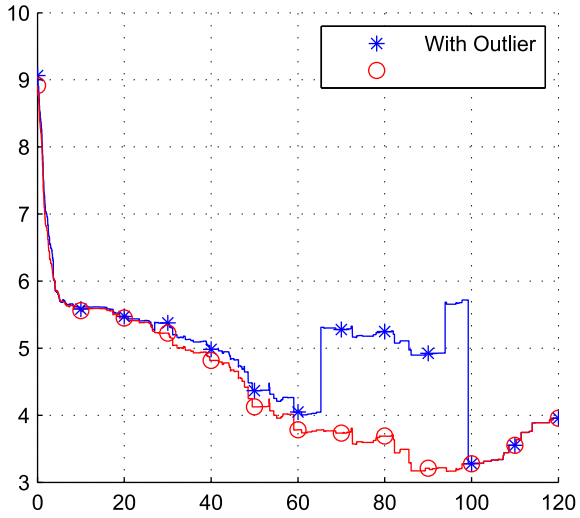

Figure 2.10. RMSE for Experiment A with and without the outlier point.

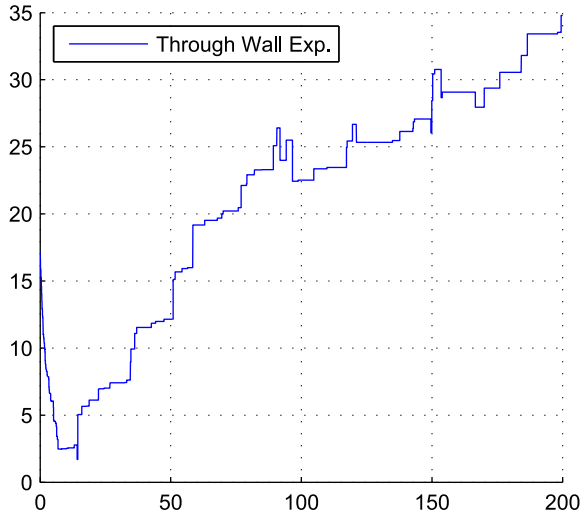

Figure 2.11. Performance of *first threshold crossing* method for the through-wall experiment

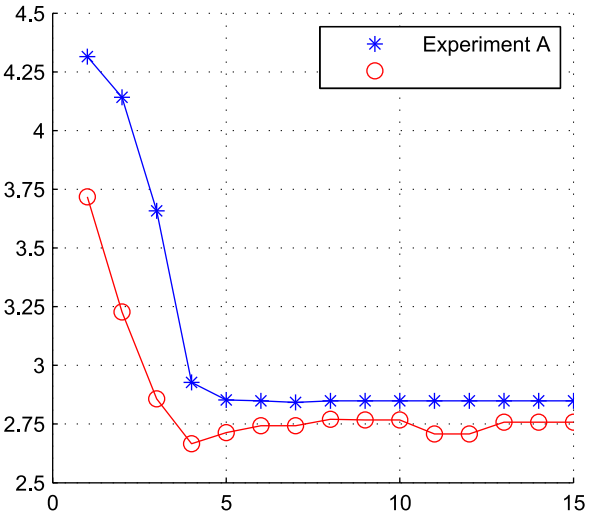

Figure 2.12. Performance of HMM-based estimator of k_* as a function of iteration count.

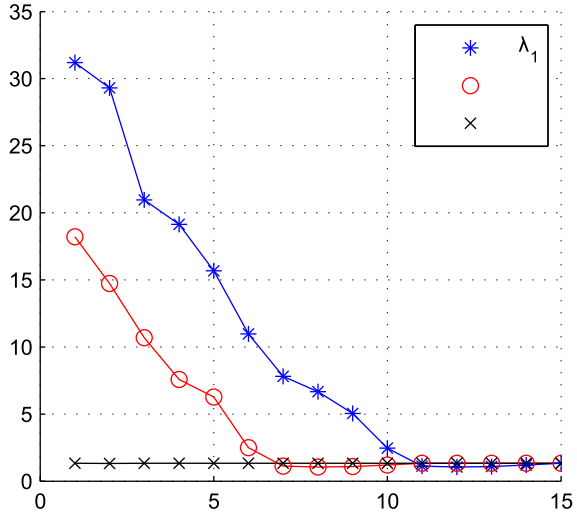

Figure 2.13. The RMSE for the through-wall experiment converges to 1.33 ns for each of the initial choices of λ derived from the data for each of the three rooms.

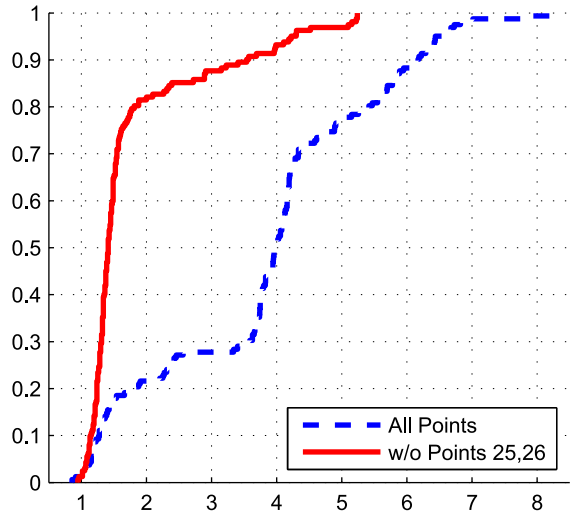

Figure 2.14. Variance of the estimator based on which set of empty room samples is used.

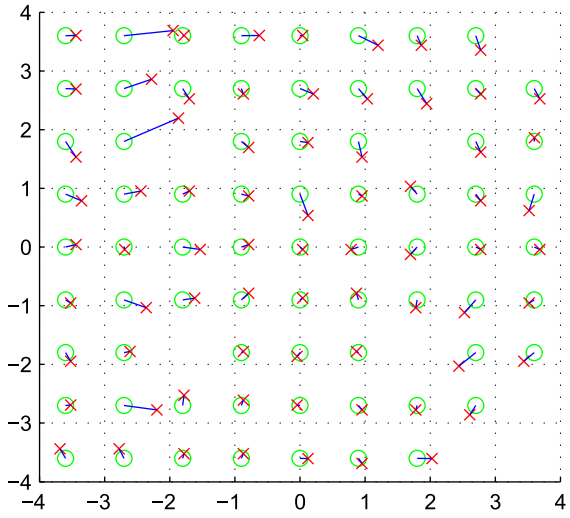

Figure 2.15. MEB 3325 actual person positions (O) and localization estimates (X) using the forward solving method.

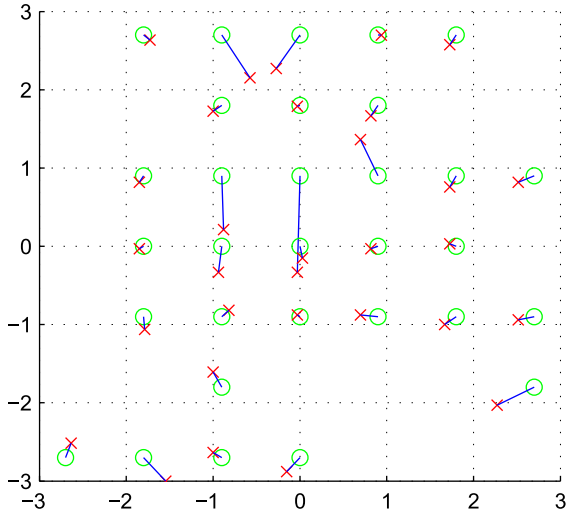

Figure 2.16. MEB 3325 actual person positions (O) and localization estimates (X) using the forward solving method..

CHAPTER 3

JOINT ULTRA-WIDEBAND AND SIGNAL STRENGTH-BASED THROUGH-BUILDING TRACKING FOR TACTICAL OPERATIONS

Accurate DFL-based on RSS measurements requires placement of radio transceivers on all sides of the target area. Accuracy degrades dramatically if sensors do not surround the area. However, law enforcement officers sometimes face situations where it is not possible or practical to place sensors on all sides of the target room or building. For example, for an armed subject barricaded in a motel room, police may be able to place sensors in adjacent rooms, but not in front of the room, where the subject would see them. In this paper, we show that using two UWB impulse radios, in addition to multiple RSS sensors, improves the localization accuracy, particularly on the axis where no sensors are placed (which we call the x-axis). We introduce three methods for combining the RSS and UWB data. By using UWB radios together with RSS sensors, it is still possible to localize a person through walls even when the devices are placed only on two sides of the target area. Including the data from the UWB radios can reduce the localization area of uncertainty by more than 60%.[1]

3.1 Introduction

Device free localization systems can be used in tactical operations or crisis situations to help emergency personnel know where people are in a room or building before they enter [8]. These systems do not require people to participate in the localization effort by wearing or carrying sensors or radio devices. Systems based on radio frequency measurements are

[1]

particularly appropriate for *e.g.* hostage or barricade situations because RF penetrates (nonmetal) walls. However, in many such situations, it is not possible to place sensors on all sides of the building or area. For example, some sides of a building might have windows where an armed subject may be watching, and deploying sensors on that side could expose police to harm or escalating the situation. As another example, a room on an upper floor of a building may have some accessible interior walls (*e.g.*, in a hallway), but the exterior wall may be unaccessible simply because of its height. This paper presents a system that expands the possibilities for RF-based DFL systems where an area cannot be surrounded with sensors by combining RSS-based DFL methods with bistatic UWB impulse radar methods.

We are particularly motivated by discussions with our local SWAT team, who have unfortunately faced three situations in as many years in our metro area [40]–[42] in which hostages were taken by a barricaded subject in a hotel or motel room. Knowing the location of the suspect represents very valuable information in planning the actions (*e.g.*, forced entry) required to bring the standoff to an end safely. In such situations, sensors could be placed in adjacent rooms to the barricaded room, but rooms have front windows, and sometimes back windows; thus, front and back walls are potentially off limits.

A DFL system based on RSS measurements [4]–[7] typically has radio transceivers, which we call *RSS sensors* placed on all four sides of a target area. RSS measurements of the links connecting every pair of sensors are used to estimate the location of the person in the room in real time. The localization process is based on models for the change in RSS introduced by the presence of a person on or near the *link line*, that is, the straight imaginary line connecting the transmitter and receiver [5], [34], [43]. When RSS sensors are placed only on two opposite sides of a room, the links cross the monitored area along one axis but not the other. This significantly degrades the localization accuracy of the system, especially along the axis with no crossing links [5].

UWB radios can be used for DFL through walls and can be accurate on the order of centimeters or tens of centimeters [12], [44]. Multiple UWB radios cooperating in a multistatic radar configuration can provide an unambiguous localization estimate [12]. A transmitter broadcasts a UWB impulse and receivers capture the time-domain CIR of the environment. Changes to the CIR are detected, and the time delay beyond the line-of-sight (LoS) pulse for each of these changes is used to estimate the range of the target from the radios [3]. These radios, however, can be prohibitively expensive to install on a permanent basis: a single UWB impulse radio can cost thousands of dollars, and using only a single

pair of radios provides insufficient information to unambiguously localize a target.

In this paper, we introduce a joint DFL system that uses the changes measured in RSS and CIR to localize and track a target, such as a person, through walls. We demonstrate, in particular, the localization accuracy of a system which deploys sensors only on two opposite sides of a room. We call the axis parallel to the sides of the room without sensors the X axis and the axis parallel to the sides of the room with sensors the Y axis (see Figs. 3.1 and 3.2). The RSS sensors primarily provide the information about the target's y coordinate, while the UWB radios primarily provide information about the target's x coordinate. This removes the need to have RSS sensors on all four sides of a target room and reduces the number of UWB radios required for localization.

In this paper we introduce methods to process and combine the RSS and CIR data in order to provide a unique position estimate. The experimental results collected in two deployments, *i.e.*, a study room at the University of Utah and a motel room in Salt Lake City, show that the joint RSS-UWB DFL system can accurately localize a noncooperative target through walls. Even when the number of deployed devices is low, *e.g*, only two UWB radios and six (three per side) RSS sensors, the system can still provide a position estimate accurate enough to reliably indicate in which part of the room the person is located. In tactical situations where the only opportunity to have access to the target room is to open a breach in a wall with an explosive frame, this information can be used by police forces to decide which wall has to be detonated and avoid hurting or killing the suspect.

In tactical operations or crisis situations, law enforcement may not have the possibility of calibrating the systems used for DFL in stationary conditions (*i.e.*, when no person is located in the target area). Thus the methods used to process the data coming from the RSS sensors and UWB radios should be able to localize and track the suspect in the room from the start, making DFL a *plug-and-play* type of system. In this paper, we propose novel variance-based methods for RSS and CIR measurements that can localize the person without requiring an initial calibration of the system in stationary conditions.

This is a proof of concept study to show the performance capabilities of a system that combines UWB information with RSS based localization techniques. In order to be practical for law enforcement personnel, the system should be able to be quickly deployed, and as such, we also study the performance of the proposed methods as a function of the number of sensors required to be deployed.

This work does not address multiple target tracking. This is a future area of research. This has been a topic of research for RSS based localization [34]–[39], but the UWB

techniques used in this work have not been designed for multiple target range estimation.

At the time of writing, there are several commercially available through-wall radio technologies that can help law enforcement determine the position of people inside a room. The Prism200 from Cambridge Consultants [45] is a through-wall radar system for determining the location and movement of people for law enforcement or emergency personnel. The Xaver^{TM} products from Camero are also through-wall UWB solutions that provide similar capabilities [46]. Time Domain is another company that offers solutions for target localization and tracking using UWB radios [47]. The UWB radios used in this work are a pair of P220 UWB radios from Time Domain. Compared to these products, the joint RSS-UWB DFL system described in this paper is considerably less expensive, as the RSS sensors cost a few tens of dollars each and only two UWB radios are required. Moreover, the compact size and low weight of the RSS sensors and UWB radios make our system easier to be installed.

The paper is organized as follows. In Section 3.2, we describe the radio RTI technique used to process the RSS measurements coming from the RSS sensors. In Section 3.3, we describe the methods used for estimating the bistatic range of a target using UWB radios by modeling the changes to the CIR as a hidden Markov model. Section 3.5 describes a target tracking scheme. Section 3.4 introduces three methods to combine the RSS and CIR data in order to provide a unique position estimate. Section 3.6 describes the experiments carried out, while Section 3.7 presents the results and compares the performance of the different methods. Conclusions are given in Section 3.8.

3.2 Radio Tomographic Imaging (RTI)

In RTI, originally introduced in [5], static radio transceivers placed at known positions form a wireless mesh network and collect RSS measurements that can be used to localize and track a person in real time without requiring the person to wear or carry any sensor or radio device. RTI can provide submeter localization accuracy, also in through-wall scenarios [8], [10], [48]. The RSS measurements of all the links of the network are processed in order to estimate a discretized image $\mathbf{x}$ of the change in the propagation field of the monitored area caused by the presence of a person. The estimation problem can be defined as:

$$\mathbf{y} = \mathbf{W}\mathbf{x} + \mathbf{n}, \tag{3.1}$$

in which $\mathbf{y}$ and $\mathbf{n}$ are $L \times 1$ vectors of the RSS measurements and noise of the L links of the network, respectively, and $\mathbf{x}$ is the $N \times 1$ image to be estimated, where N is the number of

voxels of the image. Each element x_n of $\mathbf{x}$ represents the change in the propagation field due to the presence of a person in voxel n. The $L \times N$ weight matrix $\mathbf{W}$ represents a spatial impact model between the L links of the network and the N voxels of the image. The model used in RTI [5], [8], [10], [43] is an ellipse having the foci located at the transmitter and receiver of the the link. The voxels located within the ellipse have their weight set to a constant which is inversely proportional to the root distance between the transmitter and receiver, while the voxels located outside of the ellipse have their weight set to zero.

3.2.1 Attenuation-based RTI

For attenuation-based RTI (AB-RTI) we use the method introduced in [10]. In this section, we briefly present this method and the terminology that will be used also in the following sections.

The RSS of link l on channel c at time instant k, $r_{l,c}(k)$, can be modeled as:

$$r_{l,c}(k) = P_c - L_{l,c} - S_{l,c}(k) + F_{l,c}(k) - \eta_{l,c}(k), \quad c \in \mathcal{F}, \tag{3.2}$$

where P_c is the transmit power, $L_{l,c}$ the large scale path loss, $S_{l,c}$ the shadowing loss, $F_{l,c}$ the fading gain (or *fade level* [34]), $\eta_{l,c}$ the measurement noise, and $\mathcal{F} = \{1, \ldots, H\}$ is the set of measured frequency channels. Both the large scale path loss $L_{l,c}$ and the shadowing loss $S_{l,c}$ change very slowly with the center frequency. In our experiments, we use IEEE 802.15.4-compliant transceivers [49] which may transmit in one of 16 channels across the 2.4 GHz ISM band. Because the band, 80 MHz, is small compared to 2.4 GHz, we can assume that both $L_{l,c}$ and $S_{l,c}$ are independent of the frequency channel c. Consequently, $F_{l,c}$ can be calculated as:

$$F_{l,c}(k) = r_{l,c}(k) - P_c + \eta_{l,c}(k). \tag{3.3}$$

Due to the measurement noise $\eta_{l,c}$, the fade level can not be measured directly. Thus, we estimate it by using the average RSS, $\bar{r}_{l,c,}$, measured during an initial calibration of the system performed when no person is in the monitored area:

$$\bar{F}_{l,c} = \bar{r}_{l,c} - \min_{c} \bar{r}_{l,c}. \tag{3.4}$$

In [34], the links are divided in *antifade* and *deep-fade* links depending on the change in RSS measured when a person crosses the *link line*, *i.e.* the imaginary straight line

connecting the transmitter and receiver. A link is in a deeper fade on channel c_1 than on channel c_2 if $\bar{r}_{l,c_1} < \bar{r}_{l,c_2}$. By definition, $\bar{F}_{l,c} \geq 0$ and $\bar{F}_{l,c} = 0$ for one channel c on each link. Antifade links are the most informative for localization, since their spatial impact area is limited around the link line, while deep-fade links measure a consistent change in RSS even when the person is far from the link line. For this reason, for each link l we calculate the fade level in (3.4) of each channel $c \in \mathcal{F}$, and we rank the measured frequency channels from the most antifade to the most deep-fade. If $\mathcal{A}_i$ is the set of size m containing the indices of the m top channels in the fade level ranking, the link RSS measurement y_l at time k is calculated as:

$$y_l(k) = \frac{1}{m} \sum_{c \in \mathcal{A}_i} \Delta r_{l,c}(k), \tag{3.5}$$

where $\Delta r_{l,c}(k) = r_{l,c}(k) - \bar{r}_{l,c}$, *i.e.*, $\Delta r_{l,c}(k)$ is the difference between the current RSS measurement of link l on channel c and the average RSS measured during the initial calibration phase.

3.2.2 Variance-based RTI

We present a new multichannel version of variance-based RTI (VB-RTI) extending and improving the results of [8]. In this new method, we also include the concept of fade level.

The attenuation-based RTI method in [10] requires an initial calibration of the system in stationary conditions, *i.e.*, when the monitored area is empty. Moreover, if the environment changes, *e.g.*, when the suspect in the room moves furniture or other objects, the RTI system would need to be recalibrated or would otherwise lose accuracy. The work in [48] addresses this issue and introduce methods capable of estimating the baseline RSS of the links online.

In tactical operations, such as when an armed person has barricaded himself in a house or motel room before the arrival of police forces on the scene, we cannot expect to require an empty area. Variance-based RTI can be applied in this scenario. The change in RSS due to the presence of a person on the link line can be quantified as the unbiased sample variance of the last N_s RSS measurements:

$$\hat{s}_{l,c}(k) = \frac{1}{N_s - 1} \sum_{p=0}^{N_s - 1} \left(r_{l,c}(k-p) - \mu_{l,c}(k) \right)^2, \tag{3.6}$$

where

$$\mu_{l,c}(k) = \frac{1}{N_\mu} \sum_{p=0}^{N_\mu - 1} r_{l,c}(k-p) \tag{3.7}$$

is the mean of the last N_μ RSS measurements of link l on channel c, where $N_\mu > N_s$ to be able to estimate the mean RSS of each channel on a longer time window and to filter the changes due to the person crossing the link line. Variance-based RTI does not require an initial calibration of the system and can adapt at run-time to eventual changes in the environment. For each link l, $\mu_{l,c}(k)$ in (3.7) provides an estimate of the fade level of channel c at time k. As for attenuation-based RTI in Section 3.2.1, the channels are ranked from the most antifade to the most deep-fade. The link measurement y_l at time k is calculated as:

$$y_l(k) = \frac{1}{m} \sum_{c \in \mathcal{A}_i} \hat{s}_{l,c}(k). \tag{3.8}$$

3.2.3 RTI Image Estimation

Since the number of links L is considerably smaller than the number of voxels N, the estimation of the image $\mathbf{x}$ is an ill-posed inverse problem that can be solved through regularization. In this work, we use a regularized least-squares approach [10], [43], [48], [50]. The discretized image of the change in the propagation field of the monitored area is calculated as:

$$\hat{\mathbf{x}} = \mathbf{\Pi}\mathbf{y}, \tag{3.9}$$

where $\mathbf{y} = [y_1, \ldots, y_L]^T$, and

$$\mathbf{\Pi} = (\mathbf{W}^T\mathbf{W} + \mathbf{C}_x^{-1}\sigma_N^2)^{-1}\mathbf{W}^T, \tag{3.10}$$

in which σ_N is the regularization parameter. The elements of the *a priori* covariance matrix $\mathbf{C}_x$ are calculated by using an exponential spatial decay:

$$[\mathbf{C}_x]_{ji} = \sigma_x^2 e^{-\|\mathbf{v}_j - \mathbf{v}_i\|/\delta_c}, \tag{3.11}$$

where σ_x^2 is the variance of voxel measurements, and δ_c is the voxels' correlation distance. The linear transformation $\mathbf{\Pi}$ is computed only once before the system starts operating in

real time. The calculation of $\hat{\mathbf{x}}$ in (3.9) requires $L \times N$ operations and can be performed in real time. Table 3.1 indicates the values of the parameters of the RTI image estimation process.

3.3 Ultra-wide Band Range Estimation

Assuming an UWB transmitter sends a pulse $\delta(t)$, each CIR is measured as:

$$h(t) = \sum_i \alpha_i \delta(t - \tau_i), \tag{3.12}$$

where α_i and τ_i are the complex amplitude and time delay of the ith multipath component, respectively. The line of sight path delay is τ_0. The path delay of the target, which we wish to estimate, is τ_*. We will consider a discrete-sampled version of the signal energy, r_k:

$$r_k = \int_{(k-1/2)T}^{(k+1/2)T} |h(t)|^2 dt, \tag{3.13}$$

where T is the sampling period and k ranges from $1 \dots M$ discrete periods. In this work, $T = 1\,\text{ns}$. From now on, CIR time delays will be considered only over discrete time intervals k rather than continuously on t.

3.3.1 Changes to the CIR as a Hidden Markov Model

The changes to the UWB CIR are modeled as a hidden Markov chain. We will refer to this method as *HMM-UWB* or hidden Markov model (HMM) based UWB. A hidden Markov chain is one whose states, $X_k = i$, are not directly observable but are inferred from other observation signals, O_k, available from the system. The distribution of the observation signals is dependent on the state of the system, *i.e.*, $f_{O,i} = P(O|X = i)$. To estimate the probability the system is in a given state at any time k, *i.e.*, $P(X_k = i|\mathbf{O}, \lambda)$, we need to know the distributions of the observation signals, the initial state probabilities π_i, and the state transition probabilities, $P_{i,j}$, all of which are described by $\lambda = [\pi_i, P_{ij}, f_{O,i}]$ [27].

The observations, O_k, are the difference between the CIRs of the static environment and the CIRs of when a person is located in the monitored area. This difference is calculated as the symmetric Kullback-Leibler divergence, also known as relative entropy [26]. The distribution of the observations is approximately a log-normal distribution [16].

If the changes to the CIR are modeled as a hidden Markov chain, the CIR goes from an unchanged state, $X = 0$, to a changed state, $X = 1$, at the time delay corresponding to the

time traveled by the UWB pulse from the transmitter to reflect off of the target and then arrive at the receiving radio, *i.e.*, k_* which is equivalent to τ_*. By applying this model to the system, standard HMM solving algorithms, such as the forward-backward algorithm [27], can be used to estimate when the system state changes and, thus, when changes to the CIR occur. The forward-backward algorithm determines the most likely state of the system at any given time as:

$$\hat{X}_k = \arg\max_i P(X_k = i|\mathbf{O}, \lambda). \tag{3.14}$$

These state estimates are used to estimate k_* as

$$\hat{k}_* = \{k_*|\hat{X}_k \neq 1 \forall k < k_*\}. \tag{3.15}$$

The work in [3] describes in further detail the method for estimating UWB bistatic range and its improved performance over other methods. From now on, we will let $\alpha_k = P(X_k = 1|\mathbf{O}, \lambda)$. α_k describes the probability those CIRs possibly affected by a person at time k are in the affected state. These probabilities are used to form the UWB localization image.

When solving the forward-backward algorithm, accurate estimates of when state changes occur are dependent on how well λ models the true system parameters. A known λ from another environment can be used as an initial estimate for λ when solving for the state estimates. The Baum-Welch algorithm can then help tune λ to more closely match the true parameters and improve range estimates [3], [27].

In this work, we assume there are no major changes to the environment throughout each trial that would require new calibration CIRs to be captured. This allows us to use just one calibration period for estimating k_*.

One possible way to eliminate the calibration requirement for HMM-UWB is to use the CIRs that immediately precede the CIRs with a possible target. This, however, may introduce bias and make static targets harder to detect.

3.3.2 Variance-based UWB Range Estimation

An alternative method is to use the short-term variance of the CIR for each r_k. We refer to this method as variance-based UWB (VB-UWB). α_k is calculated as:

$$\alpha_k = \frac{\sigma^2_{r_k}}{g_{r_k}}, \tag{3.16}$$

where the variance $\sigma^2_{r_k}$ is the unbiased sample variance of r_k over the N_U most recent CIRs. In this work, we let $N_U = 5$, corresponding to the number of CIRs captured in approximately 0.5 s. The normalization coefficient g is calculated as:

$$g = g(1 - \beta) + r_k\beta. \tag{3.17}$$

This is equivalent to applying a low-pass infinite impulse response (IIR) filter to r_k. In this work, $\beta = \frac{1}{N}$. Because the variance of r_k is high when the mean of r_k is high and vice versa, we normalize the variance $\sigma^2_{r_k}$ by the mean of r_k. In this way, α_k increases only when the person moves. This method is used in conjunction with the variance-based RTI method described in Section 3.2.2. The primary advantage of this method is that no calibration is required to solve for α_k. A disadvantage is that the target can disappear if it remains motionless over a long period of time. We alleviate this problem by applying the tracking method in Section 3.5.

3.3.3 UWB Image Estimation

When estimating the UWB image, the image space is constrained to contain only the inner dimensions of the target room plus one additional voxel on each image edge. Discretizing the image space into N voxels, the image vector is:

$$\mathbf{l}^u = [l^u_1, \ldots, l^u_N]^T, \tag{3.18}$$

where each voxel l^u_n has a bistatic range to the UWB transmitter and receiver described by its path delay k_n. The value of each voxel, l^u_n, is calculated as the non-negative difference function:

$$l^u_n = (\alpha_{k_n} - \alpha_{k_n - 1})^+, \tag{3.19}$$

where the non-negative difference function is defined as:

$$(x)^+ = \begin{cases} x & \text{if } x \geq 0 \\ 0 & \text{if } x < 0, \end{cases} \tag{3.20}$$

and assuming $\alpha_0 = 0$.

3.4 Combining RTI and UWB Information

In this section we introduce three methods to combine the RSS and UWB data. We compare the results of the different methods in Section 3.7.

3.4.1 Image Combination by Product

An RTI image is formed as described in Section 3.2.1 after every RSS sensor has transmitted a packet on all channels in $\mathcal{F}$, *i.e.*, after RSS measurements have been collected on all the links and channels. A UWB image is formed for every new CIR captured. In this method, the two images are combined to form the new image L^c by performing a voxel-wise product,

$$L^c = l^r \wedge l^u, \tag{3.21}$$

where $l^r = \hat{\mathbf{x}}$ from (3.9) and l^u is from the UWB image $\mathbf{L}^u$. We define $M_{L^c} = \max(L^c)$. When no person is located in the monitored area, M_{L^c} has a very low value. We use a threshold T_e to avoid further processing images not showing the presence of a person in the target area: if $M_{L^c} \leq T_e$, we discard the current combined image and wait for the next one formed by the system. Otherwise, we normalize the values of the voxels of l^r and l^u such that their minimum value is zero and the sum of all voxels is one:

$$[\hat{l}^r]_n = \frac{{l^r}_n}{\sum_{i=1}^{N} {l^r}_i}, \tag{3.22}$$

and similarly for l^u:

$$[\hat{l}^u]_n = \frac{{l^u}_n}{\sum_{i=1}^{N} {l^u}_i}. \tag{3.23}$$

The normalization brings the two images in the same range of values and weights them equally. The normalized combined image $\hat{L}^c$ is calculated again by performing a voxel-wise product of $\hat{l}^r$ and $\hat{l}^u$:

$$\hat{L}^c = \hat{l}^r \wedge \hat{l}^u. \tag{3.24}$$

The voxel-wise product is used because both images cover the same geographic region. If we consider the normalized values of the images as probabilities, the product of the two

values for each voxel pair would give the probability of the both UWB and RSS "events" occurring in that voxel. This can be done because the error in the estimates are statistically independent.

The RSS and UWB data collected by the two systems are time stamped to allow synchronizing the two images. Images are formed at the same rate as the higher of the two sampling rates. In our case, since the UWB CIRs are sampled more frequently than each RTI cycle, a combined image is formed for each new UWB sample. This image will then be the combination of the most recently formed RTI with the new UWB image. From the normalized combined image, $\hat{L}^c$, the position of the person is estimated as:

$$\hat{p} = \arg\max_{n \in N} \hat{L}^c, \tag{3.25}$$

i.e., the person's position estimate is at the voxel n having the highest value.

3.4.2 Linear Inversion with UWB Data

An alternative method to form a combined image is to modify the weight matrix $\mathbf{W}$ in (3.1) to include the UWB measurements in the inversion process. We define a new matrix $\mathbf{W}_U$ as an $M \times N$ matrix where M is the maximum value of k and N is the number of voxels of the image. The n-th column of $\mathbf{W}_U$ represents the ideal vector of α_k if the target were located at voxel i. The vector y_U is the estimated vector of α_k from the results of the forward-backward algorithm. Equation (3.1) then becomes:

$$\begin{bmatrix} \mathbf{y}_R \\ \mathbf{y}_U \end{bmatrix} = \begin{bmatrix} \mathbf{W}_R \\ \mathbf{W}_U \end{bmatrix} \mathbf{x} + \begin{bmatrix} \mathbf{n}_R \\ \mathbf{n}_U \end{bmatrix} \tag{3.26}$$

where the subscripts R and U correspond to the matrices derived from the RSS or UWB data, respectively. The inversion matrix is calculated as in (3.10) using the combined matrix $\mathbf{W}^C$. A combined localization image $\hat{L}^c$ is then formed by multiplying the combined inversion matrix $\mathbf{\Pi}^C$ to the combined RSS and UWB measurement matrix $\mathbf{y}^c$. The position of the person is estimated as in (3.25).

3.4.3 Estimating X by Using Y

The third method we propose for combining the UWB and RTI images is to derive one coordinate of the position estimate of a target from each image. First, we estimate the target location from the RTI image formed as described in Section 3.2.1. The y-coordinate from this position estimate is then used to derive an x-coordinate from the UWB image,

which is calculated as described in 3.3.3. If the target location estimate from the RTI image is at coordinates $(\hat{x}^R, \hat{y}^R)$, we consider the row of the UWB image corresponding to $\hat{y}^R$. The target position estimate $\hat{p}$ is set at the voxel having the maximum value in that row, *i.e.*, $\hat{p} = (\hat{x}^U, \hat{y}^R)$.

3.5 Localization and Tracking

The position estimate $\hat{p}$ is used for updating an already existing track of a person or for initiating a new one if the target area is empty. To this purpose, we use track confirmation and deletion rules [51]. If at time k the set of *candidate tracks*, $\mathcal{T}_d$, and the set of *confirmed tracks*, $\mathcal{T}_f$, are both empty, the position estimate $\hat{p}(k)$ is used to start a new candidate track, which is added to $\mathcal{T}_d$. A candidate track becomes a confirmed track only if its position has been updated at least h_{app} times in the last H formed images ($h_{app} \leq H$). If this condition is not fulfilled, the candidate track is deleted.

A circular *gating area* of radius ω is centered at the target's position estimate $\hat{p}$. The radius ω is defined as an integer multiple of the voxel width p. We define $\mathcal{T}_g \supseteq (\mathcal{T}_f \cup \mathcal{T}_c)$ as the set of tracks (either candidate or confirmed) located within the gating area. Only the tracks in $\mathcal{T}_g$ are considered. The confirmed tracks in $\mathcal{T}_g$ are given priority over the candidate tracks: the current position estimate is used to update the closest confirmed track. Otherwise, if no confirmed track exists, the current position estimate is used to update the closest candidate track. If the set $\mathcal{T}_g$ is empty, the current position estimate is used to start a new candidate track. By using the gating area, we avoid the position estimate of the person to have large sudden changes in correspondence of noisy RSS and CIR measurements from the two systems.

3.6 Experiments

The first experiment was conducted in a $27\,\mathrm{m}^2$ study room on the second floor of the Warnock Engineering Building at the University of Utah. A total of 33 RSS sensors were placed outside of the room along two opposite walls, 17 on one side and 16 on the other. The sensors were 30.5 cm apart. Two UWB radios were placed on one of the two sides of the room where the RSS sensors were positioned. The UWB radios were 1 m apart. A person walked along a predefined path six times, three times counterclockwise and three times clockwise. The person entered and exited the room in each of the six trials. With the help of a metronome and markings on the floor, the person walked at a constant speed of 0.5 m/s. Fig. 3.1 shows the setup of the tests carried out in the study room.

The second experiment was conducted in a $28\,\mathrm{m}^2$ room of a motel in Salt Lake City, Utah. The layout of this room is described in Fig. 3.2. This time, ten RSS sensors were placed along each of the walls separating the room from the adjacent ones. Two UWB radios were placed outside one wall of the target room. The experiments were conducted with the UWB radios at two different distances, 0.9 m and 2.7 m apart. A person walked along a predefined path at a constant speed of 0.5 m/s, entering and exiting the room each trial. There were no other rooms adjacent to the target room besides the two where sensors were placed. For the second experiment, a person walked the target path 18 times. Six of the trials were done with the UWB radios in configuration A and twelve in configuration B, represented by white stars and black stars, respectively, in Fig. 3.2.

3.7 Results

The following results are derived from data collected empirically in the study room and hotel room. This data collection was described in Section 3.6. The methods described previously were applied to this data. In the case of the study room, there were at least 16 RSS-based radios, or RSS sensors, available on each side of the room. There were 10 available on each side of the hotel room. To better understand how the performance varied with the number of available RSS sensors, the methods described were applied to the data multiple times, each time using a subset of the collected data. The results were averaged for a given number of RSS sensors. This was done to simulate the performance of the system using a fewer number of radios than were actually used. All simulations in the following results are performed in this manner (*i.e.*, using subsets of the available empirical data).

Performance is measured by the root mean square (RMS) error of the target's location estimate relative to the true location in units of meters. For AB-RTI and HMM-UWB, calibration measurements are required. For VB-RTI and VB-UWB, no calibration measurements are required.

3.7.1 Study Room

For the first experiment, 50 simulations were run using randomly selected subsets of S RSS sensors available on each side of the room. The density of sensors on each side of the target room is higher than what would be used in a typical deployment. Subset sizes for these simulations ranged from 3 to 10 sensors per side. The same subset of sensors was used for each of the six trials and remained the same when UWB radio data was included for a given simulation. The gating algorithm described in Section 3.5 was applied in all simulations. Simulations were performed using AB-RTI, AB-RTI with HMM-UWB,

VB-RTI, and VB-RTI with VB-UWB.

Fig. 3.3 shows the mean RMS localization error for each of the methods used. Each point on the figure is the error averaged over the 50 simulations and 6 trials, measured using S sensors.

The Y-axis error improves significantly with each additional sensor used on each side of the room. There is also little improvement in the Y-axis error as a result of including the UWB information. Variance-based methods show improvement in reducing Y error over attenuation-based methods. The X-axis error improves as a result of including more RSS sensors on each side of the room but not as greatly as does the Y-axis error. The improvement as a result of including UWB information, however, is much more significant and is also almost constant with the number of RSS sensors. The localization error, that is, the Euclidean distance (L^2), improves overall by 51 cm and 33 cm, on average, for attenuation and variance-based methods, respectively.

For comparison, if a point in the room is selected at random at each time, the RMS L2 error is 2.94 m on average over the 6 trials. Errors for the X and Y axes by selecting random locations are 1.65 m and 2.44 m, respectively. The tracking algorithm is not applied when using random coordinates.

3.7.2 Hotel Room

For the second experiment, 50 simulations were also run using randomly selected subsets of S RSS sensors on each side of the room for each simulation. When $S = 10$, however, only one simulation was performed because there was only one possible combination of $S = 10$ radios per side. For each simulation, localization was performed using AB-RTI, AB-RTI with HMM-UWB, VB-RTI, and VB-RTI with VB-UWB. The tracking algorithm described in Section 3.5 was also applied to each of these methods. Fig. 3.4 shows, from left to right, the L2, X, and Y errors when applying these four methods to the data collected over the 18 trials performed in the motel room. The reason the Y error degrades when including VB-UWB to VB-RTI is that VB-RTI gave noisier range estimates than HMM-UWB did. This is due to the greater signal attenuation in the hotel versus the study room and the additional environmental variations of furnishings.

One noticeable difference between the results of the two experiments is that the Y error in the second experiment decreases significantly by including VB-UWB with VB-RTI whereas for the first experiment the Y error was effectively the same. Generally, however, the same trends are visible in the results for the second experiment. The Y error improves with increasing S, and including UWB data significantly improves X error.

For the second experiment, the error using 10 sensors per side is higher than the error using 7 sensors, in many cases. There were only 10 sensors on each side of the room and, therefore, only one unique simulation could be performed using 10 sensors. By performing many simulations using subsets of the available sensors, the effect of sensor placement on localization error could be minimized. This was not possible in the case where $S = 10$ for the second experiment.

Table 3.3 shows the mean RMS error over the 18 trials performed for this experiment using all 20 RSS sensors. For comparison and as an estimate of the upper bound on error for a given environment and target path, random image coordinates are selected as the target location estimate. At each time when a combined image would be formed, X and Y coordinates are randomly selected and are used as the location estimate at that time. The gating algorithm described in Section 3.5 is not applied when randomly choosing location estimates. The results from applying the methods described in Sections 3.4.2 and 3.4.3 are also given in Table 3.3.

Note in Table 3.3 that when performing localization using AB-RTI or VB-RTI, the X-axis error is about the same as that obtained from randomly guessing an X coordinate for each image. This is critically important for tactical operations. Having some knowledge about the person's coordinate in each axis is essential for law enforcement personnel to be able to make tactical decisions.

Of the three combination methods described in Section 3.4, the image product method proposed in Section 3.4.1 performed the best.

3.7.3 Area of Uncertainty

We define the area of uncertainty (AoU) as the ratio of the L2 mean squared error (MSE) to the total area of the monitored room:

$$AoU = \frac{\text{L2 MSE}}{\text{Room Area}}. \tag{3.27}$$

Table 3.4 shows the percent reduction in the AoU by adding UWB data to AB-RTI and VB-RTI for $S = 3$ and $S = 10$ sensors.

The percent reduction in the AoU is significant except for VB-RTI in the motel room using 3 sensors. This may be due to the particular subsets of sensors used in the simulations when $S = 3$. The reduction in the AoU confirms that by adding UWB data the system can more accurately indicate to law enforcement personnel in which part of the room the person is located.

3.8 Conclusions

In this work, we present a joint DFL system that uses the changes measured in RSS and UWB CIR to localize and track a person through walls. We target tactical operations and crisis situations where it is not possible for the police forces to place sensors on all sides of the area to be monitored. Experimental results show that including UWB with RSS data significantly improves localization accuracy when RSS sensors are only available on two sides of the target area. Where RSS sensors have been placed along the Y axis, improvements in accuracy along the X axis by including UWB data are especially significant. Without including UWB data, the accuracy along the X axis can be as bad as randomly guessing an X coordinate.

We introduce three methods to combine the information from the UWB and RSS systems and we compare their performance. The multichannel variance-based RTI method proposed in this work, which does not require an initial calibration in stationary conditions, is as effective or more effective than attenuation-based RTI for through-wall localization. The improvements in localization accuracy and the reduction in the AoU demonstrate that UWB data should be included in a DFL system for tactical operations where RSS sensors may only be placed on two sides of a room.

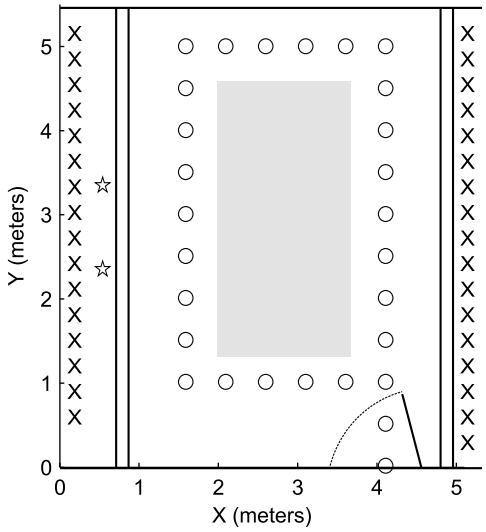

Figure 3.1. Layout of the study room located in the Warnock Engineering Building at the University of Utah used for the experiments. Xs represent the 33 RSS sensors. Stars represent the 2 UWB radios. Circles represent the steps taken by the person at one second intervals. Grey rectangles represent furniture. The target room's inner dimensions are 3.82 m by 5.49 m (21 m^2 area).

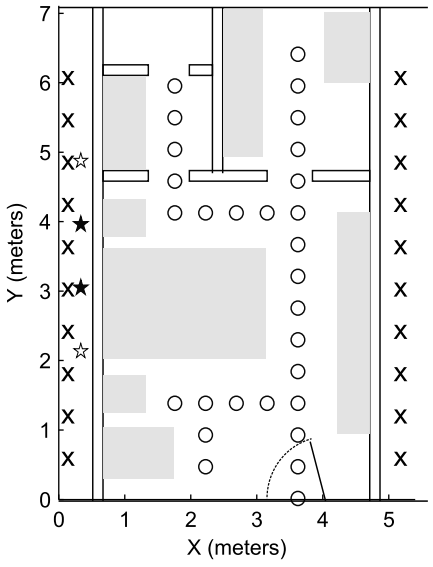

Figure 3.2. Layout of the room of a motel located in Salt Lake City, Utah. Xs represent the RSS sensors. White and black stars represent the UWB radios in configurations A and B, respectively. Circles represent the steps taken by the person at one second intervals. Grey rectangles represent furniture. The target room's inner dimensions are 3.96 m by 7.11 m (28 m^2 area).

Table 3.1. RTI image estimation parameters

Description	Parameter	Value
Voxel width [m]	p	0.15
Ellipse excess path length [m]	λ	0.02
Voxels' variance [dB]	σ_x^2	0.05
Noise standard deviation [dB]	σ_N	1
Voxels' correlation distance	δ_c	4
Number of selected channels	m	3
Short-term RSS variance window	N_s	5
Long-term RSS mean window	N_μ	50
Empty area intensity threshold	T_e	0.05
Number of updates for confirmation	h_{app}	8
Confirmation window	H	15
Gating area radius [m]	ω	1.2

Table 3.2. UWB estimation parameters

Description	Parameter	Value
Voxel width [m]	p	0.15
Sampling Period [ns]	T	1
Short-term CIR variance window	N_U	5
Variance normalization parameter	β	$1/N_U$

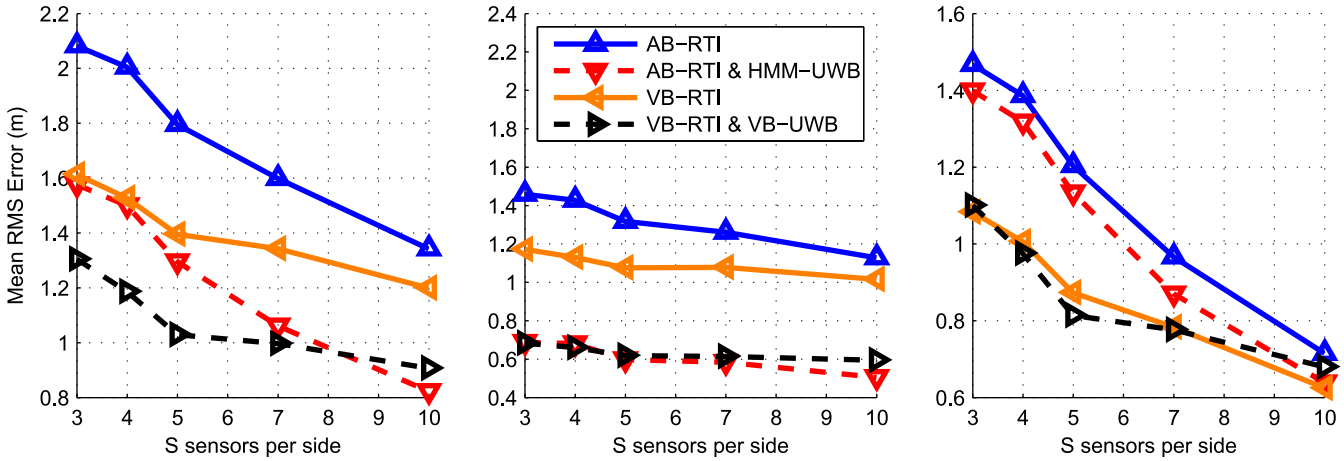

Figure 3.3. From left to right, the mean RMS L2, X, and Y errors over the 6 trials and 50 simulations using random subsets of S sensors per side of the study room.

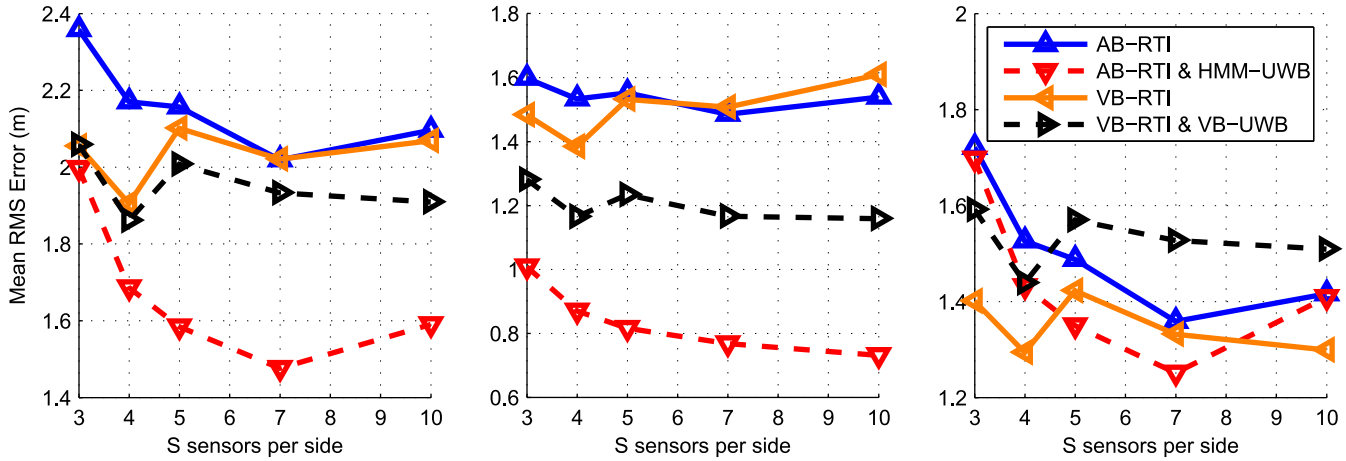

Figure 3.4. From left to right, the mean RMS L2, X, and Y errors over the 18 trials and 50 simulations using random subsets of S sensors per side of the motel room. When $S = 10$, only 1 simulation was performed.

Table 3.3. Mean RMS localization error for the second experiment over all 18 trials for the methods described. Gating was used for all methods except random selection. Units given in meters.

	Random	AB-RTI	AB-RTI & HMM-UWB	VB-RTI	VB-RTI & VB-UWB	Inversion with UWB	X from Y
L2	3.31	2.10	1.59	2.07	1.91	1.84	1.76
X	1.53	1.54	0.73	1.61	1.16	1.31	0.98
Y	2.94	1.42	1.41	1.30	1.51	1.28	1.44

Table 3.4. Percent reduction of AoU by including UWB data.

	Study Room		Motel Room	
	AB-RTI	VB-RTI	AB-RTI	VB-RTI
$S = 3$	40.2%	32.4%	26.3%	0.2%
$S = 10$	61.8%	43.2%	41.3%	14.9%

CHAPTER 4

PARALLEL MULTICHANNEL TRANSMISSION FOR RSS-BASED RADIO TOMOGRAPHY

4.1 Introduction

Device-free localization using RTI uses radios surrounding a target environment to sense and locate people within the environment. These radios take RSS measurements as sensor data. These measurements can be used to estimate the location of a person or multiple people within the environment [4]–[7]. A number of models have been developed that describe how a person affects RSS measurements depending on the location of the person and depending on the RSS levels normally measured when no person is present [4], [5], [8]–[10].[1]

Typically the method for collecting RSS measurements employs a round-robin or time division multiple access (TDMA) protocol [4], [5], [8]–[10], sometimes called spin [52] or multispin [10] which uses multiple channels. This protocol is for one radio to transmit while all other radios receive. Once the transmission ends, the next radio transmits while all others receive. This TDMA protocol continues until all radios get a turn to transmit, at which point the process repeats.

The number of turns, or time slots, needed to complete one cycle of spin or multispin is N or NM, respectively, where N is the number of radios and M is the number of channels selected for measuring. The radios in this work use about 3.5 ms per time slot. For a typical network with 25 radios using 4 channels, one complete cycle of multispin

[1]Reprinted, with permission, from M. McCracken, M. Bocca, and N. Patwari. "Selection of Links in Multichannel RSS Measurements for Radio Tomography", (to be submitted to arxiv.org and to be included in "Large Scale, Device Free Localization" by the A. Luong, M. McCracken, M. Bocca, and N. Patwari to be submitted to The 12th International Conference on Mobile Systems, Applications, and Services (MobiSys 2014)).

would require approximately 350 ms while spin, which uses only one channel, would require approximately 87.5 ms. It has been shown that multispin achieves a lower localization error than does spin, which uses just one channel [10]. A trade off is that the latency of location estimates is larger for multispin due to the larger number of measurements that are required.

The spin and multispin protocols are illustrated in Figs. 4.1 and 4.2, respectively. In these examples there are 8 radios in the sensor network. Each row represents a single radio. Each column represents a time slot in the protocol. The transmitting radio is represented with a "T" and all other radios in that time slot are receiving. The transmitting or receiving channel for each radio at each time slot is represented by the color. Once each protocol ends, it repeats from the beginning. The links between the transmitter and the receivers in the spin and multispin protocols can be visualized spatially as shown in Fig. 4.3.

The information transmitted in each transmission packet is not critical to the measurement of RSS values. Any packet transmission can be used to measure RSS. The transmission, however, is leveraged as a method to report received RSS measurements from all other radios to a central location where processing is performed. Packet length is proportional to the number of nodes, N, in the network. The duration of each time slot must be greater than a packet duration, so the slot duration is also $\mathcal{O}(N)$. Longer packets require longer transmission times, which necessarily makes the time required to complete one cycle of spin or multispin longer.

Energy consumption could be measured as the energy required by the sensor network to produce one localization estimate. By this measure, the energy consumption is proportional to the number of time slots. In this work, a Texas Instruments CC2531 system-on-chip is used for each radio. The power required during either a transmission or reception is approximately 100 mW. Multispin, in this case, requires M times more energy than spin to produce a localization estimate.

The central question answered in this chapter is the following: "In one slot, is it best to measure every link from one transmitter, or is it better to allow multiple transmitters to operate in parallel, even though doing so reduces the number of link-channels measured?" We show that using parallel transmitters can be used to dramatically improve accuracy compared to spin for the same latency and energy consumption, or to dramatically reduce either energy consumption or latency for similar accuracy compared to multispin. This is achieved by modifying the protocol, or sensor sampling schedule, to sample links that are most likely to improve localization accuracy. Fig. 4.4 is an example of a custom

protocol, or custom schedule, that differs from spin or multispin. Multiple transmitters are allowed during each time slot with transmissions performed on different channels. Not all transmitter-channel combinations are necessarily used over the N time slots used in the schedule or over the schedule cycle. The receivers are divided between the transmitters with the goal of sampling the best links of those that are available from the two transmitters. Again, color represents the channel used for that receiving or transmitting radio in that time slot.

The links between two transmitters and the receivers in a custom protocol can be visualized spatially as shown in Fig. 4.5. The color of the links represent the different channels used.

By allowing for multiple transmitters, the set of links that can be sampled in that time slot increases. For example, by going from one transmitter to two, the set of links to choose from when sampling goes from $N-1$ to $2(N-2)$, which is an increase for all but the most trivial number of radios in the sensor network. Multiple transmitters has the downside of sampling fewer links overall in each time slot. With two transmitters, $N-2$ links will be sampled rather than $N-1$ with one transmitter. We show that this is a trade off that is often worth making.

4.2 Related Work

A number of works have explored the need for deciding which sensors should be activated in a sensor network. Rowaihy *et al.* offer a survey of sensor selection schemes in wireless sensor networks [53]. The methods are divided into coverage schemes, target tracking and localization schemes, single task assignment schemes, and multiple task assignment schemes. Despite the different goals of the sensor selection methods, each does so with the intent of minimizing energy consumption while maintaining performance. All of the surveyed methods assume all sensors can be activated at any given time. An RF sensor network is different than the typical sensor networks for which methods were considered by Rowaihy *et al.* in that rather than each radio serving as a sensor or with a sensor, each radio pair is a sensor. The number of pairs of radios available, or the number of sensors, is $MN(N-1)/2$ for N radios and M channels. Because the radios can only transmit or receive, but not both, at any given time, there are a limited number of radio pairs or sensors that can be active at any given time. For one transmitter, there are $N-1$ radio links that are sampled because there are $N-1$ receivers. This situation is unlike a typical sensor network where all sensors can be active at once.

Gupta *et al.* [54] describe a stochastic sensor selection algorithm specifically for sensor

scheduling and sensor coverage. They intend this work for situations where a shared medium, such as sonar or radar, prohibits the use of all sensors at any given time. This is similar to this work. However, the authors assume first that only one sensor is used at any given time and, second, that it is to that advantage of the sensors to have received sensing data from other sensors. Neither of these assumptions are true in this work. Multiple sensors are activated at once by having multiple receivers for one transmitter. While there have been some notable exceptions [7], [55], typically sensor data is transmitted to and processed at a central location rather than at the radios, which is also done in this work.

So and Vaidya propose a multichannel media access control (MAC) protocol for ad hoc networks [56]. For ad hoc networks using 802.11, the multichannel hidden-terminal problem arises when radios want to communicate with each other on a seemingly open channel that is in use by one or more hidden-terminal radios. The goal of the proposed protocol is to "dynamically negotiate channels such that multiple communication can take place in the same region simultaneously, each in a different channel" [56]. This protocol improves the ability for radios to communicate with each other. The goals of this protocol, however, are different than those of RF sensing. Communication using multichannel MAC improves the throughput of individual data exchanges. Employing multiple channels for RF sensing actually reduces communication throughput in the sense that fewer links will be sampled and fewer links will be communicating at any given time. The goal of RF sensing, however, is not communication throughput but to sample link quality quickly over many radio links. Using multiple channels in RF sensing is done to allow for more link choices when determining which links should be sampled.

4.3 Device-free Localization

Device-free localization seeks to estimate the location of a person within the environment without the person carrying a device required for localization. The sensors in the environment measure changes caused by the presence of the person and use this information to estimate the person's location. In this case the sensors are transceiver pairs. Each packet reception has an associated RSS value. A transmitter and receiver pair can be thought of being connected to each other by a radio link, the line-of-sight path of the link following the imaginary line segment where each radio acts as an endpoint. The presence of a person will change the RSS values of the radio links the person is near. With a knowledge of the locations of the radios and the RSS values over time, the location of a person can be estimated and tracked over time [5], [34], [43].

Device free localization is typically done with round-robin protocol, known as spin [52] or multispin [10], where each radio gets an opportunity to transmit while all other radios receive. After all radios have transmitted, the radios can switch to and sample on a different channel with the goal of using this additional information to improve localization accuracy [10].

We assume fade level information is known for each link l on each channel c. The fade level of each link for each channel $F_{l,c}$ is obtained by measuring RSS on all links and on all channels of interest during a calibration period. During this calibration period the environment is empty, that is, no person is present in the environment. Link l is given by $l \in \mathcal{L}$, where $\mathcal{L} = \{(i,j) : i \neq j\}$ describes the set of all links between transmitter i and receiver j, where $i, j \in \mathcal{N}$ and $\mathcal{N} = 1, \ldots, N$, where N is the number of radios. Channel c is given by $c \in \mathcal{C}$, where $\mathcal{C} = \{1, \ldots, M\}$ describes the set of M channels available for communication and sampling. Fade level, $F_{l,c}$, measures the deviation of RSS values from those expected from the theoretical radio propagation model for link l on channel c. That is,

$$F_{l,c} = \bar{r}_{l,c} - P(d,c), \tag{4.1}$$

where $\bar{r}_{l,c}$ is the average RSS value measured for link l on channel c during the calibration period and $P(d,c)$ is a model for the expected RSS value for radios on channel c at a distance d apart. This is further described in [9, Sec. IV-C]. We also assume radio locations are known.

We do not assume, however, that measuring every link on every channel is necessary. We also do not assume that only one radio is allowed to transmit at a time.

The goal of device free localization is to minimize localization error under the given assumptions. Another goal is to minimize energy consumption in the sensor network. These goals are not necessarily compatible goals. The task is to determine the manner in which links are sampled such that localization error is minimized while also minimizing energy consumption.

4.3.1 Sampling Schedule

Methods such as spin and multispin employ a TDMA protocol for sampling the link RSS values. The manner in which links are sampled will be described as a sampling schedule or simply a schedule. In the case of spin, which uses one channel, the schedule requires N time

slots t where $t = 0, 1, 2, \ldots$. The schedule X at time t is given as the set of links sampled at time t on channel c, that is,

$$X(t) = \{(i, j, c) : i = (t \bmod N) + 1 \forall j \neq i\}. \tag{4.2}$$

Only one radio i transmits at time t. All others receive. The channel c remains constant. This schedule repeats every N time slots, allowing for localization estimates every N time slots. This schedule can be visualized as shown in Fig. 4.1.

Multispin employs a schedule using M channels. The value of $X(t)$ is the same as spin given in (4.2). The value of c changes as

$$c(t) = \left\lfloor \frac{t \bmod NM}{N} \right\rfloor + 1 \tag{4.3}$$

as t increases. This schedule repeats every NM time slots, allowing for localization estimates every NM time slots. This multispin schedule can be visualized as shown in Fig. 4.2.

In general, any schedule X could be described in such a manner. Under a set of constraints, we show that adopting a sensing schedule with multiple radios transmitting simultaneously, that is in one time slot t, can improve localization accuracy and allow for lower energy consumption in the sensor network. We propose a method for producing such a schedule. This custom schedule, like spin and multispin, would not change over time and would repeat once completed.

4.4 Methods

A device free localization network may be constrained in the amount of energy it can consume to produce a location estimate. It may also be constrained in the latency required to produce a localization estimate. Constraining the latency or the energy consumed constrains the length of the schedule. In this proof-of-concept work, we will constrain the schedule to use N time slots, which is the same as the length of single-channel spin, to show whether or not spin can be improved upon by allowing multiple transmitters in each time slot. Limiting the number of time slots necessarily limits the opportunities for links to be sampled on any given channel. To increase the opportunities for a link to be sampled, multiple radios will be used to transmit simultaneously during a single time slot. The trade off comes in the number of links that can be sampled in one time slot, which decreases from $N - 1$ to $N - 2$ for two transmitters. In this work we will allow for only two simultaneous

transmissions in each time slot. An area of future work would be to consider more than two simultaneous transmitters.

We assume that known system information includes radio locations and fade level information for each link on each channel. Given this information, the problem becomes formulating a schedule that will maintain localization accuracy while reducing the number of measurements required.

4.4.1 Scores

Let $p = (i, c)$ be the transmitter-channel combination for transmitter i and channel c. We define $\mathcal{P}$ as the set of all possible transmitter-channel combinations p where $|\mathcal{P}| = NM$. We also define $\mathcal{Q}$ as the set of all possible ways of pairing two transmitter-channel combinations in the same time slot. This is the subset of $\mathcal{P}^2$ where both i and c are not the same. Let q represent a valid pair of transmitter-channel combinations (p_1, p_2).

For N radios and two channels used simultaneously from M channels (where $M \geq 2$) there are B_q possible combinations of transmitters and channels that can be assigned to a given time slot where

$$B_q = 2\binom{N}{2}\binom{M}{2}. \tag{4.4}$$

For each q a score $S(q)$ is assigned to be used in determining which transmitters and channels are used simultaneously. A higher score indicates that the transmitters on their respective channels of q are more likely to sample links that will improve localization accuracy. In this work, each score S is calculated as follows.

For each transmitter-channel combination p, the fade level for each receiver is given as $F_{l,c}$ or, more explicitly, $F_{(i,j),c}$. For each pair of transmitter-channel combinations q with transmitters i_1 and i_2 we consider modified fade level values $\tilde{F}$ given by

$$\tilde{F}_{(i,j),c} = F_{(i,j),c} - \frac{1}{|\mathcal{N} \setminus \{i_1, i_2\}|} \sum_{n \in \mathcal{N} \setminus \{i_1, i_2\}} F_{(i,n),c}. \tag{4.5}$$

This is done because transmitters i_1 and i_2 would not be able to receive and thus their fade levels are irrelevant for this q. The value of $|\mathcal{N} \setminus \{i_1, i_2\}|$ is equal to $N - 2$. The value of $S(q)$ is then given by

$$S(q) = \frac{1}{N-2} \sum_{n \in \mathcal{N} \setminus \{i_1, i_2\}} |\tilde{F}_{\{i_1,n\},c} - \tilde{F}_{\{i_2,n\},c}|. \tag{4.6}$$

We'll now give a numerical example of how a score is calculated. RSS values are measured for all pairs of transceivers over all $M = 4$ channels. In this example there are a total of $N = 5$ radios. The numbers used in this example come from data sampled in the "Apartment 1" experiment described in Section 4.5. The score will be calculated for $q = ((1,1),(2,2))$, that is, transmitters 1 and 2 on channels 1 and 2, respectively. The vectors $F_{\{i,j\},c}$ are given as:

$$F_{\{1,j\},1} = [N/A, 5.0, -18.1, -10.7, -5.5]^T, \tag{4.7}$$

$$F_{\{2,j\},2} = [2.7, N/A, -6.3, -1.6, 3.8]^T. \tag{4.8}$$

The values of $\tilde{F}_{\{i,j\},c}$ are then calculated using Equation (4.5). The second term in this equation, or the subtrahend, is calculated as the mean of the values not corresponding to either transmitter, that is,

$$\frac{1}{|\mathcal{N} \setminus \{i_1, i_2\}|} \sum_{n \in \mathcal{N} \setminus \{i_1, i_2\}} F_{(i,n),c} = \frac{1}{3} \sum [-18.1, -10.7, -5.5]^T = -11.4, \tag{4.9}$$

$$\frac{1}{|\mathcal{N} \setminus \{i_1, i_2\}|} \sum_{n \in \mathcal{N} \setminus \{i_1, i_2\}} F_{(i,n),c} = \frac{1}{3} \sum [-6.3, -1.6, 3.8]^T = -1.4, \tag{4.10}$$

which, using Equation (4.5), gives the final values of $\tilde{F}_{\{i,j\},c}$ as

$$\tilde{F}_{\{1,j\},1} = [N/A, 16.4, -6.7, 0.7, 5.9]^T, \tag{4.11}$$

$$\tilde{F}_{\{2,j\},2} = [4.1, N/A, -4.9, -0.2, 5.2]^T. \tag{4.12}$$

The final score $S(q)$ is then calculated as given in Equation (4.6), which is the average of the absolute value of the difference between the $\tilde{F}$ values not corresponding to either transmitter, that is,

$$S((1,1),(2,2)) = \frac{1}{3}[|(-6.7) - (-4.9)| + |0.7 - (-0.2)| + |5.9 - 5.2|], \tag{4.13}$$

which gives the final value of $S((1,1),(2,2)) = 1.13$. This would be a very low score. For the experiments described in section 4.5, the median score was approximately 7.24 and the max score was 11.57.

With the goal of maximizing the score S, its value can be thought of as the average difference in fade level, normalized by the transmitters' average fade levels. If the average difference in fade level between two transmitters is high among the remaining receivers, this indicates that for a given receiver, one of the two transmitters has a good radio link with that receiver. This is normalized for the transmitter's average fade level to account for the environmental variation observed by each transmitter. Two transmitters on given channels would pair well together if, on average over all receivers, a given receiver has a very good fade level compared to the average for one transmitter and a very bad fade level for the other.

4.4.2 Constraints

We impose the following constraints when making a communication schedule. The same number of time slots are used as a single-channel spin. This is N slots where N is the number of radios in the network. For this proof-of-concept work, in each time slot there are exactly two transmitters chosen to broadcast simultaneously. The two transmitters sharing a time slot broadcast on two distinct channels among M possible channels. A given transmitter-channel combination p may only be assigned to a time slot once, that is, it may not be repeated over N time slots. The results given under these constraints will be described as the "Custom" method.

Constraining the custom schedule to N slots was done to make its results comparable to those of spin and multispin, whose schedules are necessarily of length N and NM, respectively. This work also only uses two simultaneous transmissions because it represents the first step in parallelizing transmissions. We would not expect more than two parallel transmitters to improve performance if having two does not. This is done with the goal of answering the questions posed: "In one slot, is it best to measure every link from one transmitter, or is it better to allow multiple transmitters to operate in parallel, even though doing so reduces the number of link-channels measured?"

Results will also be given when using the additional constraint of each transmitter being assigned at least one time slot over the N time slots. Without this constraint it becomes possible to produce a schedule where a radio never transmits and only receives over all N time slots. This prohibits the radio from reporting the RSS values it measures to a central location unless reporting is accomplished in some way other than during its transmission

time slot, such as through a wired communication channel. This method will be described as the "Constrained" method.

4.4.3 Solution Space Complexity

Once the B_S possible scores S are calculated, they must be used to optimally assign transmitters and channels to each of the N time slots. Ideally we would be able to check the value $V(X)$ of each possible schedule X by taking the sum of all $S(q)$ for each q used in the schedule over each of its N time slots. Once each schedule's value is determined, the schedule with the highest V would be used for localization. As will be shown, the size of the solution space prohibits an exhaustive search.

Due to the constraints given in assigning transmitter-channel combinations together to form a schedule, we cannot form a closed-form solution to the number of ways a schedule X can be formed. We can, however, determine a lower bound on this number given some assumptions.

A lower bound, B_L, is found when the scenario is considered where we impose further constraints where all transmitters use the same two channels and every transmitter is given exactly two opportunities to transmit. The value of B_L is given as

$$B_L = \binom{M}{2} B_B(N), \tag{4.14}$$

where $B_B(N)$ is given as

$$B_B(N) = N! - \sum_{n=1}^{N} \binom{N}{n} B_B(N-n) \tag{4.15}$$

and $B_B(0) = 1$. For $N = 25$ and $M = 4$ we obtain a lower bound for the number of possible valid schedules of approximately $3.42 * 10^{25}$.

The large number of combinations, B_L, prohibits an exhaustive search. This can be shown by the time required to perform such a search. The Tianhe-2, as of June 2013, is the world's fastest supercomputer and can perform 33.86 petaFLOPS, or $33.86 * 10^{15}$ floating point operations per second [57]. If we assume each schedule requires only one floating point operation to determine its value V, and ignore memory and input/output (I/O), then the time the Tianhe-2 would require to perform $3.42 * 10^{25}$ floating point operations would be over 32 years. It is simply not a worthwhile option to perform an exhaustive search across the solution space.

4.4.4 Choosing Transmitters and Channels

Formulating a schedule can be considered an optimization problem. In this work we use a greedy method to determine which transmitters are paired together on particular channels, that is, which q are assigned to each of the N time slots in the schedule X.

The first of N time slots in the schedule has assigned to it the pair of transmitter-channel combinations, or q, that achieves the maximum score S. The next slot then has assigned to it the q that achieved the next highest score S unless that assignment would violate any of the constraints given in Section 4.4.2. If any constraints are violated by this q, then it is not assigned to the schedule, and the q with the next highest score is considered. This assignment process continues until all N time slots have transmitters and channels assigned.

This is just one method to formulate a schedule. A number of optimization methods could be used to determine the optimal schedule given the scores S. Optimizing using S, however, assumes that S is a representation of its true value in reducing localization accuracy. If it does not match this reality, then further optimizing over S may not necessarily improve performance.

4.4.5 Alternative Score Function

If the score S does not accurately model a transmitter pairs impact in decreasing localization error, improving the score function would also improve localization error. An alterative score function is presented here. This new score function $S(q)_n$ is given as:

$$S(q)_n = \sqrt{S(q)d(q)}, \tag{4.16}$$

where $d(q)$ describes the distance between the transmitting radios of q in meters. This is the geometric mean of $S(q)$ and $d(q)$. Intuitively this means that we favor transmitters that are further apart over those that are close to one another. Results for this score function are described in Section 4.6.

4.4.6 Receiver Division

Once a transmission schedule has been made, the remaining radios, acting as receivers, must be assigned to the two channels to receive from either transmitter.

The two transmitters for the given time slot, i_1 and i_2, have calculated the average fade level between each transmitter and the remaining receivers given as

$$\bar{F}_{i,c} = \frac{1}{N-2} \sum_{n \in \mathcal{N} \setminus \{i_1, i_2\}} F_{\{i,n\},c}. \tag{4.17}$$

The transmitter with the highest $\bar{F}_{i,c}$ has the $\lceil \frac{N}{2} \rceil$ receivers with the highest fade level for that transmitter assigned to receive on that transmitter's channel. The remaining $\lfloor \frac{N}{2} \rfloor$ receivers are assigned to the remaining channel.

4.4.7 Simple Alternative Method

An alternative method for both producing a score S and for dividing receivers is proposed for comparison. Fade level is the primary consideration for this method, which we will call the "Simple" method.

The score S is calculated as

$$S(q) = \frac{1}{N-2} \sum_{n \in \mathcal{N} \setminus \{i_1, i_2\}} \max\{F_{\{i_1,n\},c}, F_{\{i_2,n\},c}\}. \tag{4.18}$$

This is simply the average of the maximum fade level observed for each receiver between the two transmitters. Two transmitters pair well together if they produce, on average, a high fade level for each receiver. Using these scores, transmitters are chosen as described previously in Section 4.4.4.

Receivers are assigned to receive from the transmitter that achieves the highest fade level for that receiver. This may result in an asymmetric receiver division among the transmitters. Results for this method are given in Section 4.6 and compared against the "Custom" and "Constrained" methods described previously. This simple method does not impose the transmitter constraint given to the "Constrained" method, as described previously in Section 4.4.2.

4.4.8 Radio Tomographic Imaging

Radio tomographic imaging, or RTI, is "the process of of estimating the changes in the propagation field of the deployed RF sensor network" [9]. RTI forms an image of the changes to the propagation field. We assume that changes to the propagation field are caused by the presence of a person. Location estimates are made where the propagation field changes the most, that is, at image maxima. Several RTI methods have previously been proposed [5], [8]–[10]. In this work, RTI is performed as described by Kaltiokallio *et al.* [9] with some modifications to account for having only a subset of all links being sampled. This method was chosen because it has the best reported accuracy to date for RTI. This "multiscale" method will briefly be described here.

Let a link-channel γ be defined as $\gamma = (l, c)$, where l is the link and c is the channel. We define Γ as the set of all measured link-channels for the given schedule. The size of the set Γ is given as G where $G < |\mathcal{L}|$ depending on the schedule.

For multiscale RTI, changes to the RSS measurements are used to model changes to the propagation field. When a person is not present, the sample mean of the RSS values on link-channel γ represents the normal or expected RSS value. This is given as $\bar{r}_\gamma$. The attenuation of link l on channel c, *i.e.*, γ, at time k can be estimated from the change in received signal strength as

$$\Delta r_\gamma(k) = r_\gamma(k) - \bar{r}_\gamma, \tag{4.19}$$

where $r_\gamma(k)$ is the measured RSS value at time k on link-channel γ.

The multiscale model relies on the change in attenuation as well as the direction of change. We define the vector $\Delta\mathbf{r}_\gamma^+ = [\Delta r_1^+, \ldots, \Delta r_G^+]$ as the vector of all positive changes in attenuation, where

$$x^+ = \begin{cases} x & \text{if } x > 0 \\ 0 & \text{otherwise.} \end{cases} \tag{4.20}$$

We similarly define the vector of all negative changes in attenuation as $\Delta\mathbf{r}_\gamma^- = [\Delta r_1^-, \ldots, \Delta r_G^-]$, where

$$x^- = \begin{cases} x & \text{if } x < 0 \\ 0 & \text{otherwise.} \end{cases} \tag{4.21}$$

The measurement vector $\mathbf{y}$ is the vector of each link's change in RSS, that is, $\mathbf{y} = [\Delta\mathbf{r}_\gamma^+, \Delta\mathbf{r}_\gamma^-]^T$. It is assumed that the attenuation of a link is the spatial integral of the propagation field of the monitored area. The monitored area is discretized into a plane of pixels. Each link's change in attenuation is assumed to be a linear combination of the changes in pixel attenuation.

$$y_\gamma = \sum_{d=1}^{D} w_{d\gamma} x_d + b_\gamma, \tag{4.22}$$

where x_d is the change in attenuation in pixel d, $w_{d\gamma}$ is the weight of pixel d for link-channel γ, b_γ is the measurement noise on link-channel γ, and D is the number of pixels in the discretized estimation image.

The weight $w_{d\gamma}$ is based on a spatial model of how a person located in pixel d affects link-channel γ. An elliptical model is used to represent this spatial relationship and has been applied in [5], [8], [10]. A matrix of weight values is given as $W = \left[\frac{W^+}{W^-}\right]$, where $w^+_{d\gamma} = 1$ if pixel d is in an ellipse of size λ^+_γ as described in [9]. We similarly define $w^-_{d\gamma}$.

When all links are considered, the changes to the propagation field can be modeled as

$$\mathbf{y} = \mathbf{W}\mathbf{x} + \mathbf{b}. \tag{4.23}$$

The vectors $\mathbf{y}$ and $\mathbf{b}$ are of length $2G \times 1$, the weight matrix $\mathbf{A}$ is size $2G \times D$, and the image estimate $\mathbf{x}$ is a vector of length $D \times 1$.

Solving for $\mathbf{x}$ directly is an ill-posed problem. A regularized least-squares approach is used as in [9]:

$$\hat{\mathbf{x}} = \mathbf{\Pi}\mathbf{y}, \tag{4.24}$$

where $\mathbf{\Pi}$ is given as

$$\mathbf{\Pi} = (\mathbf{W}^T\mathbf{W} + \mathbf{C}_x^{-1}\sigma_D^2)^{-1}\mathbf{W}^T \tag{4.25}$$

and σ_D^2 is a regularization parameter. An exponential spatial decay is used for the covariance matrix $\mathbf{C}_x$ given in [9, eq. (7)].

4.5 Experiments

Three data-collection campaigns were performed to test the proposed method and compare its performance to spin. The first was the same experimental data collected and used by Bocca *et al.* [10]. This was done in a study lounge in the Merrill Engineering Building at the University of Utah. The radios were placed outside the walls of the room. RSS data was measured over five 802.15.4 channels.

The second data-collection campaign was done in an apartment in Salt Lake City, Utah. Fig. 4.6 shows the layout of the apartment as well as radio locations and the path traveled by the person. With the aid of a metronome, a person walked along the path indicated by the arrows, starting at the red x at the bottom of the figure and ending at the red x at the top right of the figure. At the end of each arrow was a reference point for the person to use while moving along the path. The person took 20 seconds to move from one point to

another and remained at each reference point for 10 seconds. RSS data was measured over four 802.15.4 channels.

The third data collection campaign was performed in a different apartment in Salt Lake City, Utah. Three different experiments were performed in this apartment, similar to the ones described previously. In the results section these tests are individually tested and labeled under "Apartment 2" or "Apt 2".

In each experiment, the person moved more slowly than one would normally. This was done to use subsets of measurements as if they were available for simultaneous measurement. One complete cycle using a multispin protocol requires NM time slots to perform all of the measurements. The simulations using this collected data are sped up by a factor of M, that is, as if all M channels are available simultaneously. The proposed method creates a schedule that requires data to be measured simultaneously. When comparing it to multispin, the multispin simulations are also sped up by a factor of M, using only one channel in any given time slot.

4.6 Results

Both single-channel spin and multispin, using all available channels, were tested on the collected data from all experiments. In both cases, only subsets of the collected data were used. This was done to make the simulated RSS sampling from real RSS data occur at the same rate regardless of the scheduling method applied to the data.

The RMS ℓ^2 error between the person's estimated locations and actual locations over the path traveled by the person is used to quantify the error of each method applied. Table 4.1 gives the errors for each method used for each experiment. This is also given as a chart in Fig. 4.7. For single-channel spin, the average localization error over all M channels is given. For multispin using only m channels, where $m < M$, the results are given as the average error over all $\binom{M}{m}$ possible ways of selecting m channels. "Custom Schedule" or "Custom" does not require that each radio transmit in the schedule while "Constrained" does make this requirement, as discussed in Section 4.4.2. "Simple" uses the simpler score calculation and receiver division methods described in 4.4.7.

In Table 4.1 and Fig. 4.7 we can see the effect of using additional channels for multispin. In general, each additional channel measured will improve the localization accuracy. This comes at the cost of increasing the latency of localization estimates.

We can see from Table 4.1 and Fig. 4.7 that, on average over the five experiments, the "Custom" method achieves a localization error better than single-channel spin. It achieves

a localization error that's comparable to two-channel multispin while either using half the energy or providing half the latency of two-channel multispin.

Examples of estimated locations and their respective true locations are given in Figs. 4.8 and 4.9 for multispin and the "Custom" method, respectively, for Apartment 1. The RMS ℓ^2 error for these two methods for this experiment were 56.1 cm and 60.7 cm, respectively, as given in Table 4.1.

The "Custom" and "Constrained" methods are comparable when the average over all experiments is considered. The "Simple" method often performs better than single-channel spin but does not outperform the "Custom" method. In general, either custom schedule created by the method proposed in this work achieves a performance level much better than the performance of single-channel spin but does not perform better than multispin, which uses all channels. A real system, however, would probably require the constrained schedule to be able to report RSS measurements back to a central location.

The alternative score function described in Section 4.4.5 resulted in an average RMS error over the five experiments of 44.7 cm, just 0.1 cm worse than the "Custom" method. The fact that performance generally stays the same despite including more information in the score function suggests that intuition about modeling which transmitters should be chosen for a custom schedule is poor. More research is needed to determine a score function that more accurately describes a transmitter pair's impact on localization error.

4.6.1 Fade Level Optimization

This "Simple" method primarily considers fade level when producing a schedule. Let us consider a schedule where we ignore the constraints imposed on this method. We can produce a schedule that maximizes the sum of all link fade levels by choosing the top N pairs of transmitter-channel combinations q as given by their scores $S(q)$, calculated as described in Section 4.4.7. Receivers are also divided among transmitters as done using the "Simple" method.

Performing such an optimization results in the schedule that maximizes fade level using N different q. The average localization error over the five experiments when using this fade level-optimal schedule is 123.7 cm, which is much worse when compared to the "Simple" method's result of 48.8 cm. Fade level alone is insufficient to produce an optimal schedule in the sense that it minimizes localization error.

Our proposed "Custom" method is different in that it does not simply condier fade level but the score S calculated in Section 4.4.1. It also attempts to divide receivers evenly

among transmitters rather than using fade level information as the sole basis for receiver assignment.

4.6.2 Channel Diversity

The channels used are those described by the IEEE 802.15.4 standard for the 2.4 GHz band. When four channels were used for testing, the channels transmitted on were channels 11, 15, 21, and 26. Channel 18 was also included for the five channel test done in the study lounge. Channel center frequencies are 5 MHz apart for ajacent channels, making channels 11 and 26 lie 75 MHz apart.

For the results given in Table 4.1, the two-channel multispin errors given is the average over all ways of choosing two channels among the available M channels. In two of the five experiments, the best performing pair of channels were 11 and 26. This matches intuition that channels further apart, that is, with a greater difference in center frequency, are least correlated and best for improving channel diversity. Under the null hypothesis (H_0) each channel pair is equally likey to be the best pair for localization accurcy. Under our alternate hypothesis (H_1), channels 11 and 26 are more likely than other channel pairs to produce the best localization accuracy using multispin due to higher channel diversity. If we assume that the $\binom{4}{2} = 6$ ways of choosing a channel pair are equally likely to produce the best localization accuracy, then the probability of observing any channel pair is $\frac{1}{6}$. The probabilty of observing a particular channel pair (11 and 26) perform best n times in five experiments is given as

$$P(N = n) = \binom{5}{n} \left(\frac{1}{6}\right)^n \left(\frac{5}{6}\right)^{(5-n)}. \tag{4.26}$$

The value of $P(N \geq 2)$ can be solved as $1 - P(N = 0) - P(N = 1)$ and is equal to 0.196. This is encouraging but not statistically significant. With more experiments we may be able to better show the effect of channel diversity on localization accuracy.

4.6.3 Energy Consumption

The radios used in these experiments draw approximately 35 mA of current while transmitting or receiving and 20 μA of current while in a sleep state. Because a transmission and reception time slot use the same amount of energy, we can estimate a schedule's energy consumption per cycle by its cycle length. Single channel spin requires N time slots to complete one schedule cycle. Multispin requires NM time slots to complete one cycle. Our proposed method requires N cycles.

The energy consumed per cycle becomes significant when we consider the rate at which location estimates are produced. Multispin requires NM time slots to produce a location estimate. Single-channel spin and our proposed method requires only N time slots. Both of these later methods could use $N(M-1)$ time slots to be in the sleep state to produce location estimates at the same rate as multispin. On average, the localization accuracy with additional sleep states would remain the same. Only the rate at which localization estimates are produced would change.

In most of the experiments, $M = 4$, giving the proposed schedule an energy savings of 75% over multispin. On average over the five experiments, the proposed "Custom" schedule gives and RMS ℓ^2 error which is 4.6 cm worse than four-channel multispin. This is an increase in error by 11.6% on average.

4.7 Conclusion

We have shown that using parallel transmitters can be used to improve localization accuracy compared to spin for the same latency and energy consumption, or to dramatically reduce either energy consumption or latency for similar accuracy compared to multispin.

This work did not explore the possibility of having more than two simultaneous transmitters. This would increase the number of available sensors to choose from while reducing the total number of links that could be sampled at any given time. This is an area of future research.

We have shown that applying a custom schedule to RSS measurement can achieve a level of performance that is comparable to multispin while using just a minority subset of the measured data. Its performance is also better than single-channel spin, which uses approximately the same number of measurements. This shows first that employing data from multiple channels improves performance. This also shows that not all measurements are equally significant in their impact toward improving localization error.

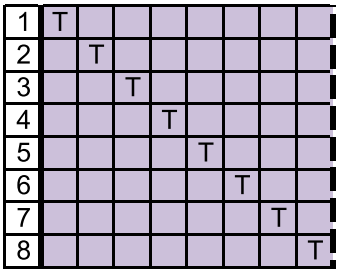

Figure 4.1. An example of the multispin protocol for 8 radios and 4 channels. Each row represents a radio. Each column represents a time slot. A "T" indicates the transmitting radio in that time slot. All other radios in that slot are receiving. The channel is indicated by color.

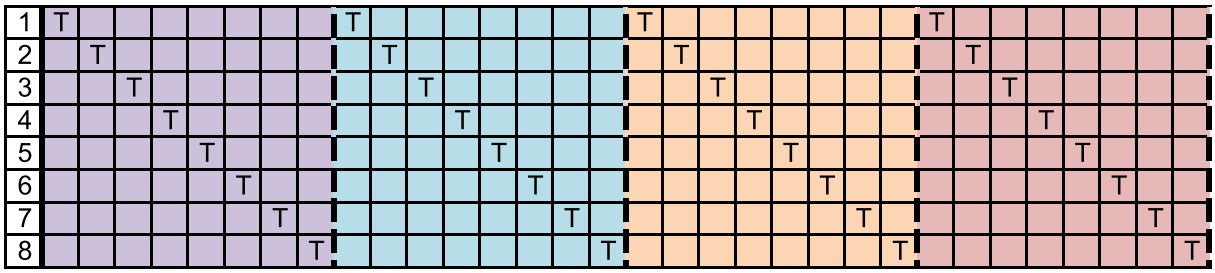

Figure 4.2. An example of the multispin protocol for 8 radios. Each row represents a radio. Each column represents a time slot. A "T" indicates the transmitting radio in that time slot. All other radios in that slot are receiving. The channel is indicated by color.

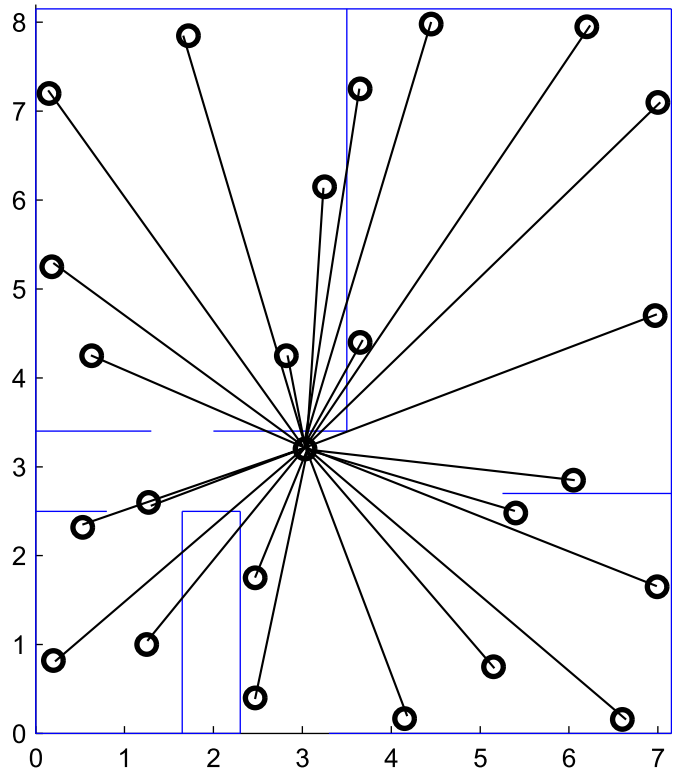

Figure 4.3. The links between transmitter and receivers can be visualized spatially for the spin and multispin protocols. This figure represents just one time slot in the protocol.

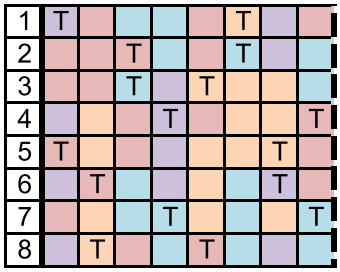

Figure 4.4. An example of a custom schedule or protocol for 8 radios and 4 channels. Each row represents a radio. Each column represents a time slot. A "T" indicates a transmitting radio in that time slot. All other radios in that slot are receiving. The transmitting or receiving channel is indicated by color.

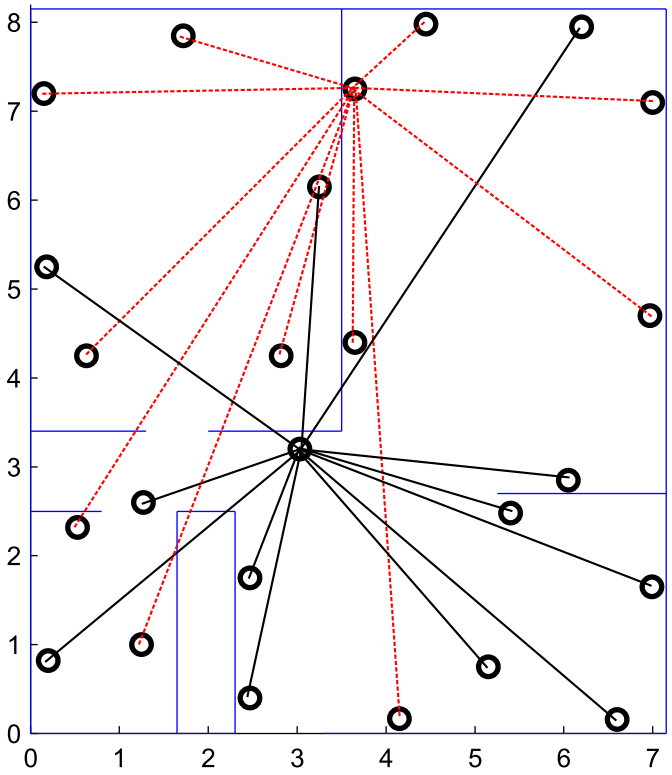

Figure 4.5. The links between two transmitters and the remaining receivers can be visualized spatially for a protocol using a custom schedule. This figure represents just one time slot in the protocol.

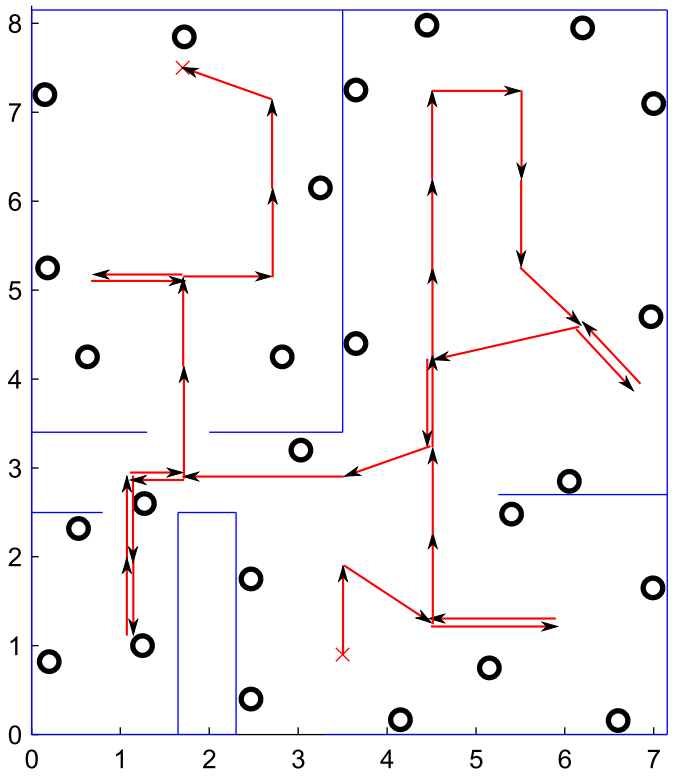

Figure 4.6. Layout of the apartment. Red x's are path endpoints, the person starting at the red x at the bottom of the figure, following the path arrows, and ending at the red x at the top left of the figure. Black circles are radio locations. Blue lines are apartment walls. Axis units are given in meters.

Table 4.1. Error of each method for all experiments given as the RMS ℓ^2 error in units of cm.

	Study Lounge	Apt 1	Apt 2 - Test 1	Apt 2 - Test 3	Apt 2 - Test 4	Average
1 Channel	59.3	74.0	52.8	43.3	49.0	55.7
2 Channel	41.9	63.8	38.6	36.4	42.1	44.6
3 Channel	35.5	58.8	38.3	36.9	42.4	42.4
4 Channel	33.8	56.1	35.6	35.3	38.9	39.9
5 Channel	29.7	N/A	N/A	N/A	N/A	N/A
Custom	33.4	60.7	44.1	40.5	44.2	44.6
Constrained	40.3	60.7	41.6	40.9	44.3	45.6
Simple	35.7	65.4	48.7	42.0	52.1	48.8

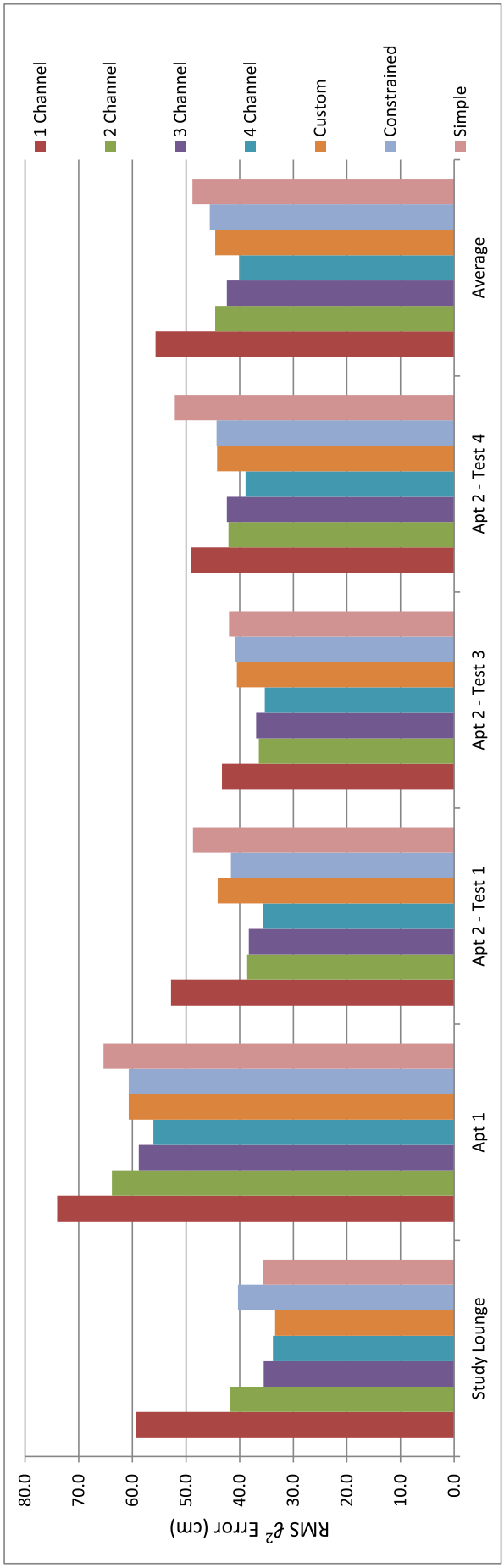

Figure 4.7. A chart of the results given in Table 4.1, excluding those for 5 channel multispin.

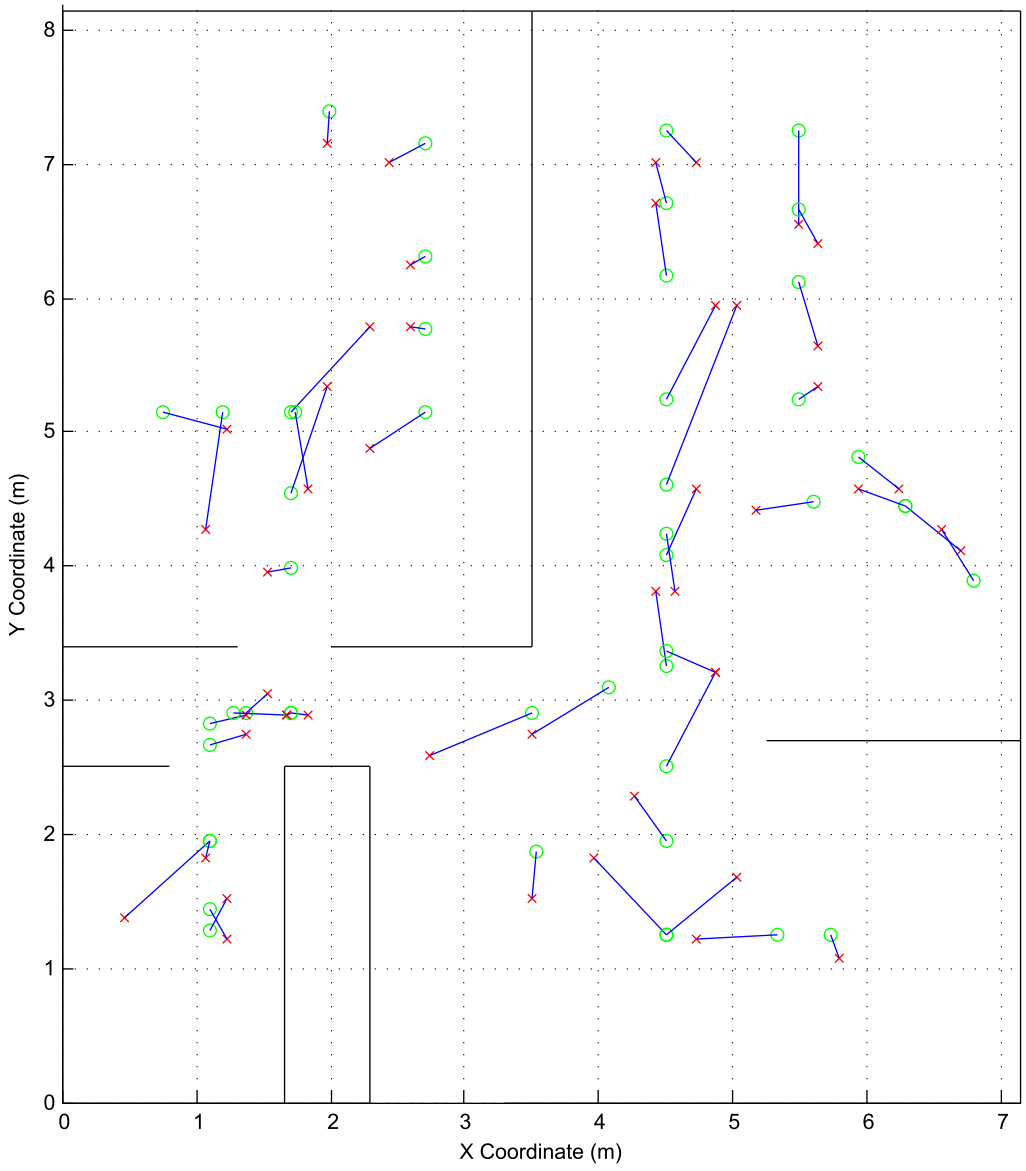

Figure 4.8. Actual person positions (O) and localization estimates (X) using multispin in Apartment 1.

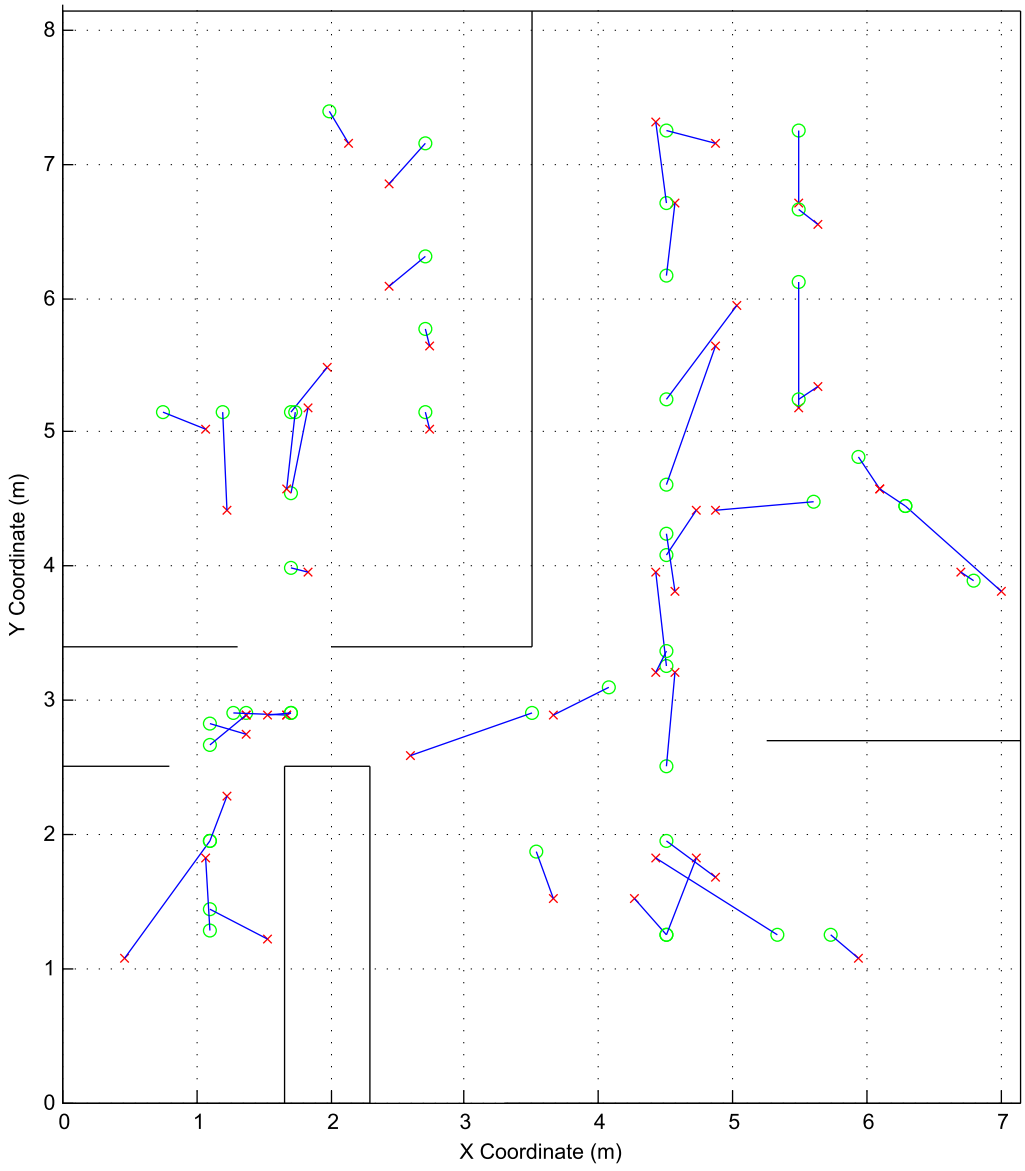

Figure 4.9. Actual person positions (O) and localization estimates (X) using a custom schedule in Apartment 1.

CHAPTER 5

CONCLUSIONS

We have shown the effectiveness of a number of methods to improve upon device-free localization using both wideband and narrowband RF sensing and how these methods can be combined. UWB ranging can still be performed for localization even when a number of common assumptions about the received signals are not true. We have shown how UWB and RSS-based localization methods can be combined to improve localization accuracy in a constrained setting. We have also shown that by having multiple parallel transmitters in RSS-based radio tomography, we can improve localization accuracy while reducing energy consumption or measurement latency.

5.1 Engineering Trade-offs

Choosing to perform RTI using either UWB measurements or RSS measurements requires that engineering trade-offs are made. These include system cost, energy consumption, and localization accuracy. A typical UWB localization system would require at least four radios, pairwise configured in a bistatic radar configuration. A typical RSS-based localization system requires on the order of 12 to 35 radios.

The two P220 UWB radios from Time Domain together cost around $7000. Newer models similarly sell between $2500 and $4000 each [58]. The radios used to measure RSS values are based on a reference design from Texas Instruments for the CC2531 system-on-chip. Several hundred were manufactured for these and other works and cost approximately $18 each.

The energy consumed by each system is important for systems that require little maintenance. The P220 UWB radios require 5.7 W of power during operation. The CC2531-based radios each require approximately 100 mW of power during operation.

In Chapter 2, it is shown that localization accuracies of 24 cm and 36 cm were achieved for two different experiments using four UWB radios. RSS-based localization methods also

achieve similar levels of accuracy [9]. A table summarizing this information is given in Table 5.1.

UWB radios perhaps could provide even greater localization accuracies than is shown in Chapter 2 by using more radios. With unit costs on the order of thousands of dollars, however, the benefits often do not outweigh the costs. An ideal scenario for employing UWB radios is described in Chapter 3 where radios of either kind can be placed on only two opposite sides of a room or target area. Only two UWB radios in a bistatic radar configuration are required in this scenario, minimizing their cost while adding localization information that would not be available otherwise. In nearly all other scenarios, RSS-based localization is preferable over UWB-based methods for the given reasons.

5.2 Future Areas of Research

There are many topics and possible modifications to this work that could lead to further future research. Some of these will be discussed in greater detail.

There are existing radios that give even more channel state information than CC2531-based radios used in the RSS-based localization work. For example, 40 MHz bandwidth channel impulse responses are available from Intel 5300 Wi-Fi cards in both the 2.4 GHz and 5 GHz bands. These provide much more information than is available from a 1 MHz narrowband radio and are much less expensive than UWB radios, costing approximately $10 for the radio card and about $300 for the host computer. Because each card is also necessarily attached to and controlled by a host computer, there is much more processing capability at each node location than the TI CC2531 SoC's can provide. These features differ from existing RF localization systems such that their value in RTI systems is worth exploring. Other such wideband radios with rich channel state information may become available in the future, as well.

For UWB radios, despite the precise, time-domain information provided, the high monetary cost of these systems cannot be ignored. Based on recent trends, it is difficult to imagine the unit cost of these radios to drop substantially in the near future. This is in part due to the difficulty in engineering UWB impulse radios. If, however, these radios are available for use in research, there are some topics for future research using these radios. Because of the large amount of information provided by the time-domain signal response from these radios and the signal response's sensitivity to changes in the environment and radio placement, secret key generation from these signal responses would be possible. This rich signal response information could also be used to more precisely model how a person

changes the channel impulse response in multiple environments. This could be helpful to create better models for narrowband localization.

The work presented in Chapter 2 does not model the effects of changes to the CIR due to the presence of multiple people in the environment. The positive impact of employing a hidden Markov model to improve bistatic range estimation could be modified to account for multiple people.

The work done to improve localization accuracy by using just a subset of the available measurements, described in Chapter 4, was done using only fade-level information to choose measurements for a custom sensing schedule. The effect a link has on localization accuracy is more than a function of fade level. It is also dependent on the environment, such as link distance, the link's proximity to or crossing of walls, the likelihood of a person approaching that link in the environment, *etc.* Its effect is also dependent on the accuracy of the model taking as inputs the RSS values measured on that link. This dependence on more than fade-level information is shown by the following example.

Using the data collected in the apartment labeled Apartment 1 in Section 4.6, many simulations were performed to see how a link impacted the performance of localization error at any given moment in time. The simulation was done as follows. For each link, two simulations were performed to see how it affected localization accuracy over time. The first was done without the link's information included and the second included the link's information. In both simulations, to exaggerate the effect that link had on performance at each moment in time, only a subset of all available links were used. In this example, only the information from 10% of the available links was included when estimating the person's location over time. This subset of links was chosen randomly. For each link this pair of simulations was performed 150 times, each time choosing a different random subset of links for comparison. In this apartment, there were 25 nodes, making $\binom{25}{2} = 300$ links per channel and 1200 total links over the 4 available channels.

Fig. 4.6 shows the path traveled by the person throughout the apartment. The person starts at the bottom red x in the figure and moves, respectively, through the kitchen, the living room, the hallway, the bathroom, and finally the bedroom where the path ends. Nodes are placed throughout the apartment. Fig. 5.1 shows the effect of each link on channel 1 over time. The horizontal axis is time and each row of pixels represents one link. Black pixels occur when the link helps reduce localization error. White pixels occur when the link makes the localization error worse at the time. Gray pixels show when the link has no effect on localization error.

There are some interesting observations from Fig. 5.1. First is that the majority of pixels are gray. Most of the time a link will not impact localization error either way. This is primarily a function of the location of the person relative to the link, which is expected from the model. Another observation is that there are two points in time, at approximately time sample 700 and at time sample 950, where the set of links that are impacting localization error change. These times correspond to when the person moved from the living room to the hallway and when the person moved from the bathroom to the bedroom. Based on the path traveled by the person, shown in Fig. 4.6, and the effect shown in Fig. 5.1, we can conclude that a link's effect is regional. The apartment could easily be divided into three regions, each region having its own subset of links that make up aid in localization accuracy. This effect was not explored in Chapter 4 but could be a future area of research. By taking into account not only fade level but also the walls in the environment, the likely locations of the person, *etc.*, additional gains in localization accuracy could be achieved.

Table 5.1. A comparison of a typical UWB localization system and a typical RSS-based localization system. Accuracy is given in units of cm. Energy is given in units of Watts.

	Accuracy	Device Count	System Cost	System Energy
UWB	30	4	$10,000	22.8
RSS	25	33	$600	3.3

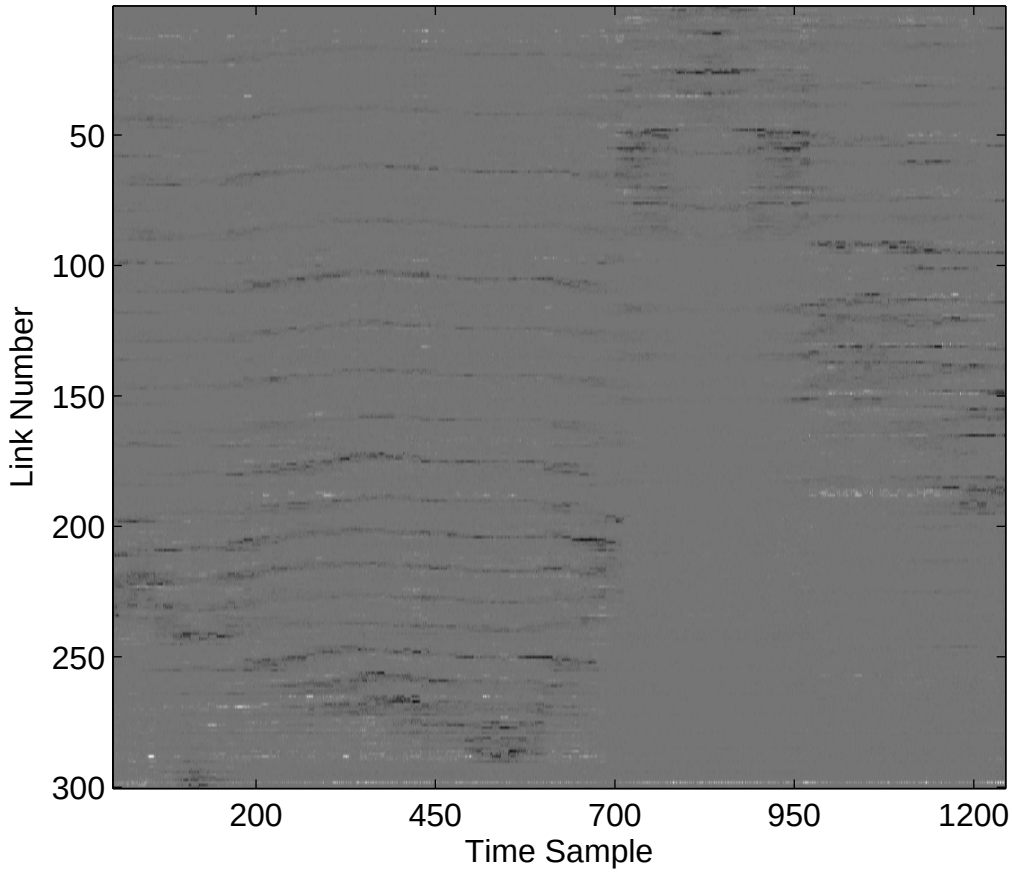

Figure 5.1. The effect each link has on localization accuracy over time in Apartment 1, which was described in Chapter 4, for each link on channel 1. Each row represents a link. Black represents improving localization accuracy, white represents hurting, and gray represents having no effect.

REFERENCES

[1] S. Khan and M. Shah, "Tracking multiple occluding people by localizing on multiple scene planes," *IEEE Trans. Pattern Anal. Mach. Intell.*, vol. 31, no. 3, pp. 505–519, 2009.

[2] B. Wagner, D. Timmermann, G. Ruscher, and T. Kirste, "Device-free user localization utilizing artificial neural networks and passive RFID," in *2012 Ubiquitous Positioning, Indoor Navigation, and Location Based Service*, 2012, pp. 1–7.

[3] M. McCracken and N. Patwari, "Hidden Markov estimation of bistatic range from cluttered ultra-wideband impulse responses," *IEEE Trans. Mobile Comput.*, to be published.

[4] M. Youssef, M. Mah, and A. Agrawala, "Challenges: Device-free passive localization for wireless environments," in *ACM Int. Conf. Mobile Computing and Networking*, 2007, pp. 222–229.

[5] J. Wilson and N. Patwari, "Radio tomographic imaging with wireless networks," *IEEE Trans. Mobile Comput.*, vol. 9, no. 5, pp. 621–632, May 2010.

[6] N. Patwari and J. Wilson, "RF sensor networks for device-free localization and tracking," *Proc. IEEE*, vol. 98, no. 11, pp. 1961–1973, Nov. 2010.

[7] O. Kaltiokallio and M. Bocca, "Real-time intrusion detection and tracking in indoor environment through distributed RSSI processing," in *2011 IEEE 17th Int. Conf. Embedded and Real-Time Computing Systems and Applications*, vol. 1, Aug. 2011, pp. 61–70.

[8] J. Wilson and N. Patwari, "See-through walls: Motion tracking using variance-based radio tomography networks," *IEEE Trans. Mobile Comput.*, vol. 10, no. 5, pp. 612–621, May 2011.

[9] O. Kaltiokallio, M. Bocca, and N. Patwari, "A multi-scale spatial model for RSS-based device-free localization," Feb. 2013. [Online]. Available: http://arxiv.org/abs/1302.5914

[10] O. Kaltiokallio, M. Bocca, and N. Patwari, "Enhancing the accuracy of radio tomographic imaging using channel diversity," in *9th IEEE Int. Conf. Mobile Ad Hoc and Sensor Systems*, Oct. 2012.

[11] M. Seifeldin, A. Saeed, A. Kosba, A. El-Keyi, and M. Youssef, "Nuzzer: A large-scale device-free passive localization system for wireless environments," *IEEE Trans. Mobile Comput.*, vol. 12, no. 7, pp. 1321–1334, 2013.

[12] R. Thoma, O. Hirsch, J. Sachs, and R. Zetik, "UWB sensor networks for position location and imaging of objects and environments," in *2nd European Conf. Antennas and Propagation, 2007.*, Nov. 2007, pp. 1–9.

[13] C. Chang and A. Sahai, "Object tracking in a 2D UWB sensor network," in *Conf. Rec. 38th Asilomar Conf. Signals, Systems and Computers*, vol. 1, Nov. 2004, pp. 1252–1256.

[14] G. Wei, Y. Zhou, and S. Wu, "Detection and localization of high speed moving targets using a short-range uwb impulse radar," in *2008 IEEE Radar Conf.*, May 2008, pp. 1–4.

[15] R. Zetik, S. Jovanoska, and R. Thoma, "Simple method for localisation of multiple tag-free targets using UWB sensor network," in *2011 IEEE Int. Conf. Ultra-Wideband*, Sept. 2011, pp. 268–272.

[16] M. McCracken and N. Patwari, "Hidden Markov estimation of bistatic range from cluttered ultra-wideband impulse responses," in *2nd IEEE Topical Meeting on Wireless Sensors and Sensor Networks*, 2012, pp. 17–20.

[17] M. McCracken, M. Bocca, and N. Patwari, "Joint ultra-wideband and signal strength-based through-building tracking for tactical operations," in *2013 10th Annu. IEEE Communications Society Conf. Sensor, Mesh and Ad Hoc Communications and Networks*, 2013, pp. 309–317.

[18] J. Taylor, *Ultra-wideband Radar Technology*, 1st ed. Boca Raton, FL: CRC Press, 2001.

[19] S. Chang, N. Mitsumoto, and J. W. Burdick, "An algorithm for UWB radar-based human detection," in *2009 IEEE Radar Conf.*, May 2009, pp. 1–6.

[20] S. Chang, M. Wolf, and J. W. Burdick, "Human detection and tracking via ultra-wideband (UWB) radar," in *2010 IEEE Int. Conf. Robotics and Automation*, May 2010, pp. 452–457.

[21] A. Giorgetti and M. Chiani, "A new approach to time-of-arrival estimation based on information theoretic criteria," in *2011 IEEE Int. Conf. Ultra-Wideband*, Sept. 2011, pp. 460–464.

[22] Y. Nijsure, Y. Chen, C. Litchfield, and P. B. Rapajic, "Hidden Markov model for target tracking with uwb radar systems," in *2009 IEEE 20th Int. Symp. Personal, Indoor and Mobile Radio Communications*, Sept. 2009, pp. 2065–2069.

[23] Z. Sun, G. Bradford, and J. Laneman, "Sequence detection algorithms for PHY-layer sensing in dynamic spectrum access networks," in *IEEE J. Sel. Topics Signal Process.*, vol. 5, no. 1, Feb. 2011, pp. 97–109.

[24] A. F. Molisch, K. Balakrishnan, D. Cassioli, C.-C. Chong, S. Emami, A. Fort, J. Karedal, J. Kunisch, H. Schantz, U. Schuster *et al.*, "IEEE 802.15.4a channel model-final report," *IEEE P802*, vol. 15, no. 04, p. 0662, 2004.

[25] B. Donlan, D. McKinstry, and R. Buehrer, "The UWB indoor channel: Large and small scale modeling," *IEEE Trans. Wireless Commun.*, vol. 5, no. 10, pp. 2863–2873, Oct. 2006.

[26] T. Cover and J. Thomas, *Elements of Information Theory*, 2nd ed., ser. Wiley Series in Telecommunications and Signal Processing. Hoboken, NJ: Wiley-Interscience, 2006.

[27] L. Rabiner, "A tutorial on hidden Markov models and selected applications in speech recognition," *Proc. IEEE*, vol. 77, no. 2, pp. 257–286, Feb. 1989.

[28] E. Paolini, A. Giorgetti, M. Chiani, R. Minutolo, and M. Montanari, "Localization capability of cooperative anti-intruder radar systems," *EURASIP J. Advances in Signal Process.*, vol. 2008, no. 1, p. 726854, 2008. [Online]. Available: http://asp.eurasipjournals.com/content/2008/1/726854

[29] S. Bartoletti, A. Conti, and A. Giorgetti, "Analysis of UWB radar sensor networks," in *2010 IEEE Int. Conf. Communications*, May 2010, pp. 1–6.

[30] S. Ergut, R. Rao, O. Dural, and Z. Sahinoglu, "Localization via TDOA in a UWB sensor network using neural networks," in *2008 IEEE Int. Conf. Communications*, May 2008, pp. 2398–2403.

[31] M. Chiani, A. Giorgetti, M. Mazzotti, R. Minutolo, and E. Paolini, "Target detection metrics and tracking for UWB radar sensor networks," in *2009 IEEE Int. Conf. Ultra-Wideband*, Sept. 2009, pp. 469–474.

[32] S. Bartoletti, A. Giorgetti, and A. Conti, "UWB sensor radar networks for indoor passive navigation," in *2012 Tyrrhenian Workshop on Advances in Radar and Remote Sensing*, Sept. 2012, pp. 140–145.

[33] Time Domain. *Ultra Wideband Ranging, Communications, & Radar.* [Online]. Available: http://www.timedomain.com/

[34] J. Wilson and N. Patwari, "A fade-level skew-laplace signal strength model for device-free localization with wireless networks," *IEEE Trans. Mobile Comput.*, vol. 11, no. 6, pp. 947–958, June 2012.

[35] D. Zhang and L. Ni, "Dynamic clustering for tracking multiple transceiver-free objects," in *2009 IEEE Int. Conf. Pervasive Computing and Communications*, March, pp. 1–8.

[36] D. Zhang, Y. Liu, and L. Ni, "RASS: A real-time, accurate and scalable system for tracking transceiver-free objects," in *2011 IEEE Int. Conf. Pervasive Computing and Communications*, March, pp. 197–204.

[37] S. Nannuru, Y. Li, Y. Zeng, M. Coates, and B. Yang, "Radio-frequency tomography for passive indoor multitarget tracking," *IEEE Trans. Mobile Comput.*, vol. 12, no. 12, pp. 2322–2333, 2013.

[38] S. Nannuru, Y. Li, M. Coates, and B. Yang, "Multi-target device-free tracking using radio frequency tomography," in *2011 7th Int. Conf. Intelligent Sensors, Sensor Networks and Information Processing*, Dec., pp. 508–513.

[39] M. Bocca, O. Kaltiokallio, N. Patwari, and S. Venkatasubramanian, "Multiple target tracking with RF sensor networks," *IEEE Trans. Mobile Comput.*, to be published.

[40] N. Bond. (2011, June) *Ogden standoff ends with gun shots.* [Online]. Available: http://www.abc4.com/s/RcPlwoCoB0yBw4mhq56SiA.cspx

[41] A. Falk. (2011, Feb.) *Police arrest two after hotel standoff.* [Online]. Available: http://www.sltrib.com/sltrib/home/51277562-76/police-hotel-lake-salt.html.csp

[42] J. Smith. (2010, July) *14-hour standoff ends with arrest.* [Online]. Available: http://www.deseretnews.com/article/700052528/14-hour-standoff-ends-with-arrest.html

[43] N. Patwari and P. Agrawal, "Effects of correlated shadowing: Connectivity, localization, and RF tomography," in *IEEE/ACM Int. Conf. Information Processing in Sensor Networks*, Apr. 2008, pp. 82–93.

[44] S. Bartoletti and A. Conti, "Passive network localization via UWB wireless sensor radars: The impact of TOA estimation," in *2011 IEEE Int. Conf. Ultra-Wideband*, Sept. 2011, pp. 258–262.

[45] Cambridge Consultants. *Prism 200.* [Online]. Available: http://www.cambridgeconsultants.com/prism

[46] Camero. *Xaver*$^{\text{TM}}$ *Tactical Through Wall Imaging Solutions.* [Online]. Available: http://www.camero-tech.com/Index.php

[47] Time Domain. *P410 MRM.* [Online]. Available: http://www.timedomain.com/p400-mrm.php

[48] O. Kaltiokallio, M. Bocca, and N. Patwari, "Follow @grandma: Long-term device-free localization for residential monitoring," in *7th IEEE Int. Workshop Practical Issues in Building Sensor Network Applications*, Oct. 2012.

[49] Texas Instruments. *A USB-enabled system-on-chip solution for 2.4 GHz IEEE 802.15.4 and ZigBee applications.* [Online]. Available: http://www.ti.com/lit/ds/symlink/cc2531.pdf

[50] Y. Zhao and N. Patwari, "Noise reduction for variance-based device-free localization and tracking," in *8th IEEE Conf. Sensor, Mesh and Ad Hoc Communications and Networks*, June 2011.

[51] S. Blackman and R. Popoli, *Design and Analysis of Modern Tracking Systems.* Boston, London: Artech House Publishers, 1999.

[52] J. Wilson and N. Patwari. (2011) *Spin: A token ring protocol for RSS collection.* [Online]. Available: http://span.ece.utah.edu/spin

[53] H. Rowaihy, S. Eswaran, M. Johnson, D. Verma, A. Bar-Noy, and T. Brown, "A survey of sensor selection schemes in wireless sensor networks," in *SPIE Defense and Security Symp. Conf. Unattended Ground, Sea, and Air Sensor Technologies and Applications IX*, 2007.

[54] V. Gupta, T. H. Chung, B. Hassibi, and R. M. Murray, "On a stochastic sensor selection algorithm with applications in sensor scheduling and sensor coverage," *Automatica*, vol. 42, no. 2, pp. 251–260, 2006.

[55] M. A. Kanso and M. G. Rabbat, "Compressed RF tomography for wireless sensor networks: Centralized and decentralized approaches," in *Proc. 5th IEEE Int. Conf. Distributed Computing in Sensor Systems*, ser. DCOSS '09. Berlin, Heidelberg: Springer-Verlag, 2009, pp. 173–186.

[56] J. So and N. H. Vaidya, "Multi-channel mac for ad hoc networks: Handling multi-channel hidden terminals using a single transceiver," in *Proc. 5th ACM Int. Symp. Mobile Ad Hoc Networking and Computing*, ser. MobiHoc '04. New York, NY, USA: ACM, 2004, pp. 222–233. [Online]. Available: http://doi.acm.org/10.1145/989459.989487

[57] L. Garber, "News briefs," *Computer*, vol. 46, no. 8, pp. 18–20, 2013.

[58] J. Hedges, private communication, Mar. 2013.